LRP 682/00 October 2000

Invited and contributed Papers
presented at the
Joint Varenna-Lausanne International Workshop on "Theory of Fusion Plasmas" Varenna, Italy, August 28th - September 1st, 2000

by the Theory Group

ISSN 0458-5895

LIST OF CONTENTS

SIMULATIONS OF IMPROVED CONFINEMENT DISCHARGES AND SAWTOOTH PERIOD WITH ECH AND CURRENT DRIVE IN TCV

C. Angioni, T.P. Goodman, Z. A. Pietrzyk, and O. Sauter

Centre de Recherches en Physique des Plasmas
Association EURATOM - Confédération Suisse,
Ecole Polytechnique Fédérale de Lausanne, 1015 Lausanne, Switzerland

Abstract

The PRETOR 1-1/2 D transport code [1] has been modified to simulate discharges with the highly flexible electron cyclotron heating (ECH) system [2] of the TCV tokamak [3]. The code has been interfaced with the TORAY ray-tracing code [4], used to determine the power deposition profile in TCV on a regular basis. In the last experimental campaigns, dedicated experiments with intense ECH have been performed clearly pointing out the effects of the power deposition profile and the current drive on the electron energy confinement and on the sawtooth activity. Discharges with Improved Central Confinement have been produced using particular heating and current drive schemes [5]. Transport simulations, with transport coefficients based on the RLW transport model [6] and a sawtooth crash model based on a critical shear value at $q = 1$ [7], already validated for ohmic discharges in TCV, [8] and [9], are in surprisingly good agreement with the experimental results. For discharges with intense central counter current drive and Improved Central Confinement, the simulation results predict an extreme sensitivity to very small changes in the location of the current drive, (i.e. within the expected error bars). This sensitivity has been confirmed by preliminary experimental results. Due to this strong sensitivity, the simulation results do not allow a conclusive validation of the transport model. However some numerical results in very good agreement with experiments have been found even when the confinement time exceeds the RLW global scaling law by a factor of 3.5. With very localized ECH power deposition profiles, the experimental sawtooth period strongly depends on the power deposition localization and on even very small amounts of current drive [10]. Performing a vertical sweep of the power deposition in the poloidal plane, the sawtooth period shows an evident maximum, which increases strongly when increasing the power density and the amount of current drive, from counter to co. The numerical results reproduce the general features of the experimental sawtooth behaviour.

1 Introduction: PRETOR and the TCV tokamak

PRETOR [1] is a predictive 1D time dependent transport code, coupled with a 2D equilibrium solver. The code includes different transport models, in particular the Rebut-Lallia-Watkins (RLW) [6], the MMM95 [11] and the IFS/PPPL model [12]. The RLW local transport model has been already applied in the transport simulations of TCV ohmic discharges, and validated over a wide range of plasma parameters [8]. The simulations of the discharges with electron cyclotron heating (ECH) and current drive (CD) presented in this paper have all been performed with the RLW local transport model. It must be

emphasized that, as these discharges are caracterized by very low densities ($n_{el19} \simeq 1$), electrons and ions are completely decoupled, and we are concerned only with the electron transport. The transport coefficient expression as well as details of the equations implemented in the code related to the connection between the transport equations and the equilibrium evolution, which are of crucial importance in the simulation of discharges with intense ECH/ECCD, will be presented later. PRETOR also includes a model for the sawtooth crash based on a critical shear value at q = 1 [7]. This model has already been applied to simulate the sawtooth period in Ohmic TCV discharges [9]. The code has been modified to take into account the highly flexible ECH system of TCV and it has been also interfaced with the TORAY ray tracing code [4]. TCV is a medium-sized tokamak (R = 0.88 m, a = 0.25 m, $I_p \leq 1$ MA) with a highly elongated vacuum vessel which can generate a unique variety of plasma shapes [3]. At the time of the experiments it was equipped with six gyrotrons at 82.7 GHz of 0.5 MW each whose polarization is adjusted to couple to the X-mode at the second harmonic. TCV is also supplied by a very flexible beam delivery system, which allows electron cyclotron power deposition at any plasma location with or without a parallel wave-vector component [2]. This experimental setup allows systematic scans in the power deposition and in the injection angles, exploring various heating and current drive configurations. In the simulation of a full discharge the following methodology is used. The code takes as input the plasma boundary, the experimental traces of the time evolution of the plasma current, the toroidal magnetic field, and the volume average electron density, as well as the power and current drive external sources. The outputs of the code are the temperature and density profiles of electrons, ions, impurity and neutrals, the current density profiles, the safety factor and the equilibrium magnetic field profiles, the loop voltage and the effective charge number. In the case of ECH/ECCD discharges, at very low density with strong central heating, the simulated electron density profiles are too peaked on axis compared with to the experimental ones, which are flat or even hollow: the RLW particle transport model, even if it gives satisfactory results for normal Ohmic discharges [8], is not adequate to reproduce the experimental density profiles in the case of intense central heating. Moreover, the experimental density behaviour with central ECH shows some features which are still under study: among these, a strong pump-out effect, [13], in particular at low triangularity ($\delta \leq 0.2$), like in the case of the shots considered in this paper. This effect is not at all included in the PRETOR particle transport model. Hence, in order to correctly concentrate our analysis on the heat transport model, we also use as an input the experimental density profiles, measured every 50 ms by a 35 chords Thomson scattering system, [14]. The ECH and ECCD sources are computed by TORAY. This code uses as input the toroidal and poloidal injection angles, the experimental electron temperature and density profiles, and it is interfaced with the TCV equilibrium reconstruction code LIUQE [15]. It provides the power absorption percentage, the CD efficiency, and the power and driven current density profiles. TORAY is run at each time slice at which the electron temperature and density Thomson scattering profiles are measured. When simulating a complete discharge, PRETOR uses the power deposition and driven current density profiles of the TORAY output in the time evolution.

In the two following subsections details will be given about the transport model adopted in the simulations and the equations implemented in the code to simulate the evolution of the self-consistent equilibrium magnetic fields and current density profiles. Then in Sec. 2 transport simulations of high confinement discharges with intense ECH/ECCD will be presented. In Sec. 3 sawtooth period simulations of discharges with poloidal sweeps of the power deposition along the resonance will show that a sawtooth crash model based on a critical shear value at q = 1 is able to reproduce the experimental dependence in ECH/ECCD operation.

1.1 The RLW local transport model

The transport model used in the simulations is essentially the original RLW transport model [6]. Slight geometrical modifications have been introduced in order to simulate the temperature profiles in the case of TCV discharges with edge safety factors above 7. The model used in all the simulations presented in this paper can be formulated as follows: the anomalous electron conductive heat flux $Q_{e,an}$ is given by

$$Q_{e,an} = -n_e \chi_{e,an} \langle |\nabla \rho|^2 \rangle \frac{\partial T_e}{\partial \rho}, \tag{1}$$

where

$$\begin{aligned} \chi_{e,an} &= \frac{C_{e,an}}{R_0^{1/2}} \epsilon^{1/2} (1 + Z_{eff})^{1/2} \left| \left(\frac{\partial_\rho T_e}{T_e} + 2 \frac{\partial_\rho n_e}{n_e} \right) \frac{q^2}{\partial_\rho q} \right| B_t^{-1} \left(\frac{T_e}{T_i} \right)^{1/2} \\ &\times \left(\frac{1}{2} + \frac{r}{a} \right)^2 \left(1 - \frac{(\partial_\rho T_e)_c}{\partial_\rho T_e} \right) \mathrm{H}(\partial_\rho T_e - (\partial_\rho T_e)_c), \end{aligned} \tag{2}$$

and

$$(\partial_\rho T_e)_c = \frac{5.5}{q} \left(\frac{\eta_{neo}\, j\, {B_t}^3}{n_e \sqrt{T_e}} \right)^{\frac{1}{2}}. \tag{3}$$

η_{neo} is the neoclassical resistivity and $\partial_\rho = \partial / \partial \rho$. H(x) is the Heaviside function. In Eqs. 2 and 3 temperatures are expressed in keV, particle densities in 10^{19} m^{-3}, the current density in MA m^{-2}, the magnetic field in Tesla and lengths in m. The coefficient $C_{e,an}$ in the simulation of TCV discharges is usually equal to 0.5 but for very low densities ($n_{el19} < 2$), like in the case of some ECH discharges, it must be increased up to 0.8. Note that the RLW thermal conductivity $\chi_{e,an}$ is inversely proportional to shear, and, in the case of negative shear, the transport reduction is taken into account only by means of the absolute value of the shear.

1.2 Self-consistent equilibrium profiles evolution

In the presence of intense ECH power and strong ECCD, the effects of the external sources on the magnetic equilibrium configuration can be significant. A correct description of the evolution of the equilibrium magnetic fields and current density profiles in the simulation of such discharges becomes extremely important. In this section the equations implemented in PRETOR to compute the evolution of the equilibrium magnetic fields and current density profiles are described. Once the temperature and density profiles have been updated, solving the flux surface averaged 1D diffusion equations reported in Ref. [8], they are used to compute the neoclassical conductivity and the bootstrap current, using formulas of Ref. [16]. Taking into account the current drive density profiles, Faraday' s law can be applied in the following form:

$$\frac{\partial B_{po}}{\partial t} = -\frac{\partial \tilde{E}}{\partial \rho} = -\frac{\partial}{\partial \rho} \eta_{neo} (\tilde{j}_{tot} - \tilde{j}_{BS} - \tilde{j}_{CD}), \tag{4}$$

where the effective poloidal magnetic field is defined as usual and the superscript tilde indicates a flux surface average operation

$$B_{po} \doteq 1/R_0 \, (d\Psi/d\rho), \qquad \tilde{E} \doteq \frac{< E_\parallel B >}{F R_0 < R^{-2} >}.$$

In the second definition, $F = 2\pi R B_\Phi/\mu_0$. In Eq. 4, the total current density profile $\tilde{j}_{tot}$ can be written in terms of the effective poloidal magnetic field by means of Ampére's law. This gives a diffusion equation for B_p in which the radial derivatives of the boostrap and driven current densities take the place of the source term, and the neoclassical resisitivity takes the place of the diffusion coefficient

$$\frac{\partial B_p}{\partial t} = -\frac{\partial}{\partial \rho}\left[\eta_{neo}\frac{F}{\mu_0 G_\Phi}\frac{\partial}{\partial \rho}\left(\frac{G_\theta B_p}{F}\right)\right] + \frac{\partial\, \eta_{neo}\,(\tilde{j}_{BS} + \tilde{j}_{CD})}{\partial \rho}, \tag{5}$$

where $G_\theta = \oint B_p dl \oint dl/B_p/\partial_\rho V$ and $G_\Phi = \partial_\rho V \oint dl/(R^2 B_p)/(4\pi^2 \oint dl/B_p)$. The new poloidal magnetic field profile is therefore computed solving this diffusion equation. Then the toroidal integrated current density profile I_t and F are updated

$$I_t = \frac{2\pi R_0}{\mu_0} G_\theta B_p, \qquad F^2 = \int \frac{2V'}{\mu_0 G_\Phi}\frac{\partial P}{\partial \rho} d\rho + \int \frac{1}{G_\theta G_\Phi}\frac{\partial I_t^2}{\partial \rho} d\rho. \tag{6}$$

The safety factor and current density profiles are then given by

$$q = G_\theta G_\Phi \frac{F}{I_t}, \qquad j = \frac{1}{2\pi R_0}\frac{F}{G_\Phi}\frac{\partial}{\partial \rho}\left(\frac{I_t}{F}\right). \tag{7}$$

The radial derivatives of the total pressure profile and of the toroidal covariant component of the magnetic field, $p'(\rho)$ and $FF'(\rho)$ respectively, are used as source terms in the Grad-Shafranov equation solved by the 2D coupled equilibrium solver. This provides the new self-consistent magnetic equilibrium and all the metric functions needed in the transport equations. In particular the flux surface average $< |\nabla\rho|^2 >$, which occurs in the heat nad particle diffusion equations, $dV/d\rho$ as well as G_θ and G_Φ.

2 Transport simulations of high confinement discharges with central ECH/ECCD

In this section we report on the simulation of four discharges, chosen to give different examples of particular heating schemes. The plasma parameters for the shots are common: elongation $k \simeq 1.7$, triangularity $\delta \simeq 0.2$, edge safety factor $q_{edge} \simeq 7$, and plasma current $I_p \simeq 200kA$. In Fig. 1 the time evolution of the electron thermal confinement time is contrasted with the RLW global scaling law [6]. The ECH power is shown below each plot. In each shot, after a starting Ohmic phase, two heating phases are performed, with different heating configurations and power: details will be given later. What we want to highlight at this stage is that, after the Ohmic phase in which the RLW global scaling is in good agreement with the experimental confinement time, the heated phases are characterized by $H_{RLW}(\doteq \tau_{E\,exp}/\tau_{RLW})$ factors which are largely above one. In particular shots ♯18639 and ♯18518, with 1.8 MW and 2.25 MW respectively, in the second heated phase have H_{RLW} factors which exceed 3. These shots are two examples of the Improved Central Confinement (ICC) [5]. Intense central counter (CNTR) CD is performed in these two cases. Indeed we have found on TCV that central CNTR-CD is particularly favourable to confinement. When compared to the same heating scheme with only heating, example given by shot ♯18604, CNTR-CD allows better plasma perfomances up to almost a factor 2 in the confinement time and more than a factor 2 in the central electron temperature. With intense central ECH and ECCD, the heating schemes must be optimized to avoid strong MHD activity and disruptions. In particular several discharges have been produced showing that some "prepared" configurations with off-axis heating, producing flat central

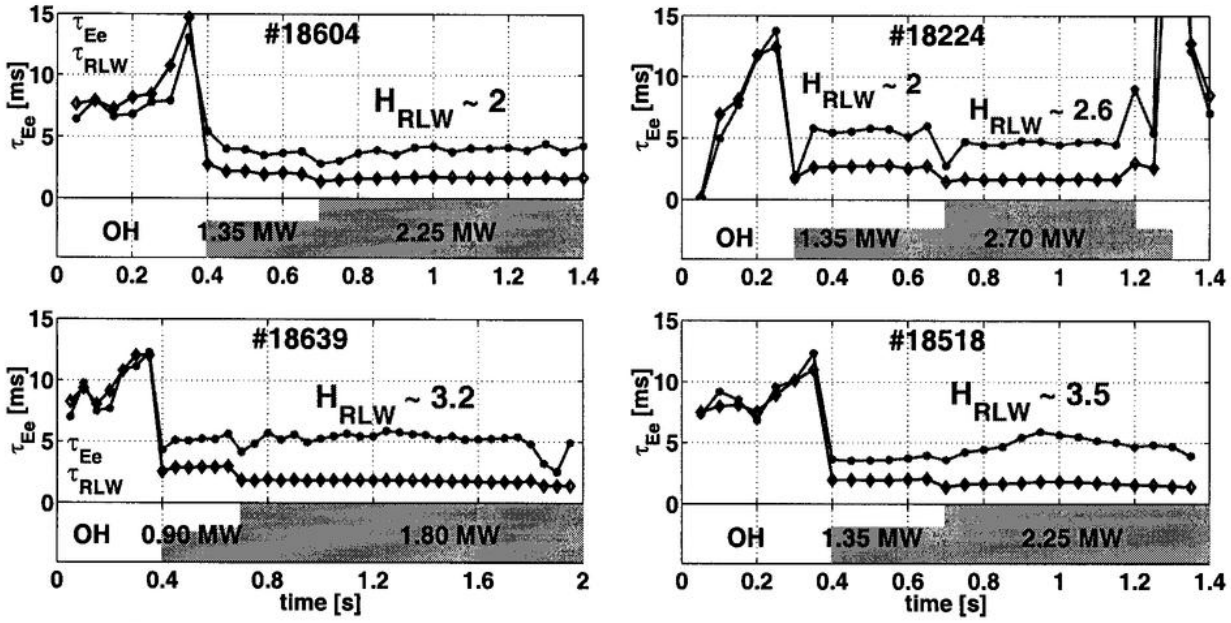

Fig. 1. *Confinement time and H_{RLW} factors for the four chosen shots*

electron temperature profiles, are suitable to allow strong internal energy improvements with very stable plasmas when the central CNTR-CD is applied: this is the ICC regime. In any case, even without central CNTR-CD, as in the case of shot ♯18604, with only heating, the H_{RLW} factor is around 2. This means that, even if the central CNTR-CD has a strong influence on the global plasma performance, an important contribution which provides a global confinement larger than the global scaling law comes from an additional effect. In the next subsection we shall show that the ECH power localization in the good confinement plasma region, namely the center, is sufficient to explain the good plasma performance shown for instance by shot ♯18604, with heating only, when compared to the global RLW scaling.

2.1 Heating only: shot ♯18604

In Fig. 2 we show the confinement time obtained with three different values of deposition width in a gaussian ECH deposition profile, with two power steps. We see that with a broad deposition profile, ($\Delta\rho = 200\%$) the RLW global scaling is recovered (the total power is renormalized to be mantained constant inside the plasma with different $\Delta\rho$). As soon as more localized power deposition profiles are considered, the confinement time rapidly exceeds the global RLW scaling. Note that these results are computed with the local RLW transport model. With $\Delta\rho = 25\%$ a H_{RLW} factor of 1.75 is found. Indeed, because the transport coefficient is usually lower in the central plasma region and larger towards the edge, only a small percentage of the power is deposited in the good confinement region in the first case, with $\Delta\rho = 200\%$, while in the case with $\Delta\rho = 25\%$ almost all the power is deposited in the good confinement region. When the local RLW transport model is applied in the simulation of a complete discharge, we see that the experimental results are well reproduced, even though the global RLW scaling is a factor 2 below the experimental confinement time. In Fig. 3 we compare the PRETOR central electron temperature with Thomson scattering and two foils experimental measurements. In this discharge a first ECH phase has been produced with 1.35 MW deposited off-axis ($\rho_{dep} \simeq 0.35$), then, after 300 ms, 0.9 MW has been added on-axis.

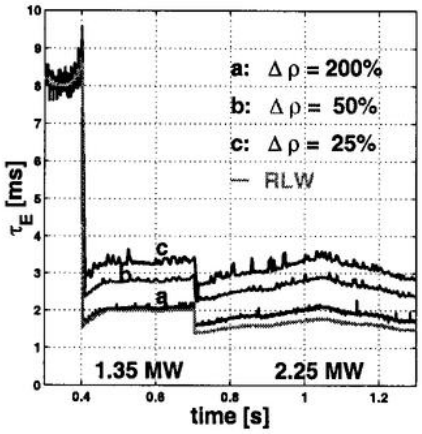

Fig. 2. *Comparison between the confinement time with three different deposition width and the RLW global scaling law*

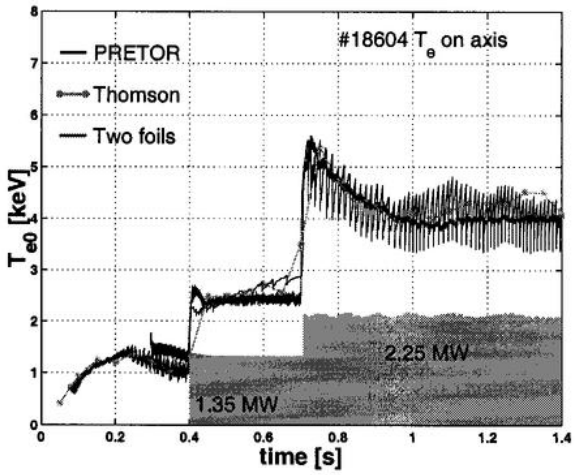

Fig. 3. *Simulated and measured T_e on-axis for shot ♯18604*

2.2 Off-axis CO-CD and on-axis CNTR-CD: shot ♯18224

In this subsection we briefly report on the simulation of a more complicated heating and CD scheme, with two power steps, the first with 1.35 MW and the second with 2.7 MW, the full available heating power. The heating scheme produces CO-CD off-axis and CNTR-CD on-axis, applied at the same time. From TORAY, the driven current is of -21 kA CNTR and 20 kA CO during the first power step, and -54 kA CNTR and 42 kA CO in the second step. The local RLW model reproduces T_{e0} in very good agreement the measured electron temperature evolution of the full discharge. In particular in Fig. 4 we show to the temperature profiles at three different time slices during the discharge, as compared with the Thomson scattering profiles. Also the corresponding safety factor profiles are shown in Fig. 5. Note that the amount of current drive is sufficient to clearly modify the safety factor profile. The computed safety factor profiles show a q = 1 surface very close to the magnetic axis, which is consistent with the very small, short period oscillations seen on the soft X-ray central chord traces.

2.3 Improved Central Confinement simulations: shots ♯18639 and ♯18518

The ICC regime, as we have already said, is obtained with a specific heating scheme. First ECH off-axis, $\rho_{dep} \simeq 0.3 \div 0.35$, is applied. This produces flat central electron temperature and safety factor profiles. In the second step on-axis CNTR-CD is added, with typically $-I_{CD} > 0.5\, I_p$. This produces the ICC regime, with very peaked electron temperature profiles (above 10 keV), very stable plasmas, low MHD activity, and high global confinement: H_{RLW} factors around 3.5. Peculiar problems are encountered when simulating these discharges. The simulation results are highly sensitive to the ECCD density profiles. Supposing a quasi steady-state situation during the ICC phase, we can assume that the parallel electric field profile is flat and its value simply given by $E_0 = V_{\rm loop}/2\pi R_0$. The relation between the steady state current density profile $\tilde{j}_{SS}$ and the current drive density profile $\tilde{j}_{CD}$ then reads

$$\tilde{j}_{SS} = \frac{E_0}{\eta_{neo}} + \tilde{j}_{BS} + \tilde{j}_{CD}, \tag{8}$$

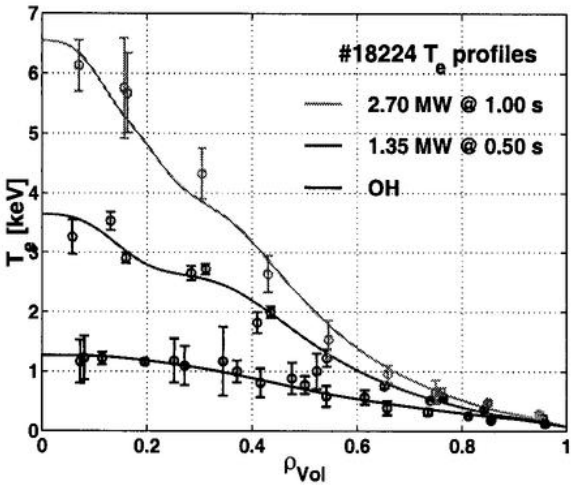

Fig. 4. *Simulated and measured T_e profiles for shot ♯18224*

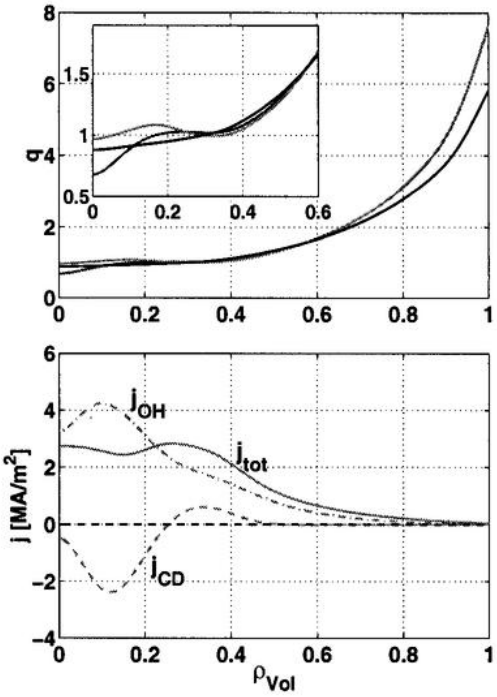

Fig. 5. *Simulated q and j profiles for shot ♯18224*

in which the first two terms of the right hand side, involving the neoclassical resisitivity and the bootstrap current, are computed from the experimental data. We have imple-

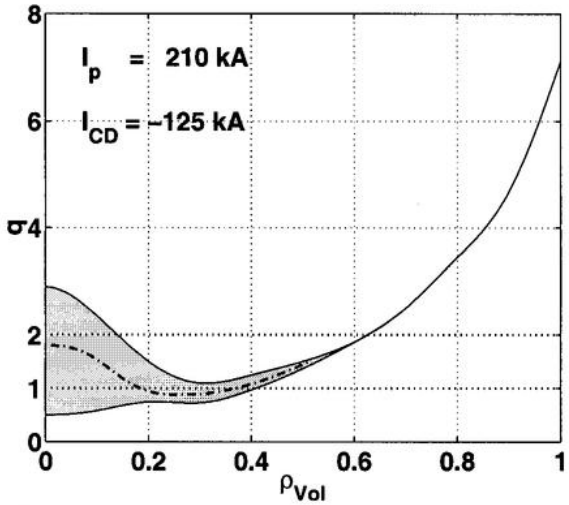

Fig. 6. *Range of steady state q profiles for shot ♯18639*

mented this simple calculation in PRETOR, and we have computed the safety factor profiles corresponding to a set of different current drive density profiles, within the expected errors. The q profiles obtained are inside the patched area presented in Fig. 6. As the RLW transport model strongly depends on the current density and safety factor profile, this uncertainty prevents the validation (or invalidation) of the transport model. Indeed when the standard simulation methodology is applied to two shots in the ICC regime, different results have been obtained. In Fig. 7 the simulated central temperature for shot ♯18639 is compared with the experimental data of Thomson scattering and two foils: the result of the transport simulation is largely below the experimental data. The temperature, current density and safety factor profiles are shown in Fig. 8. In the simulation, the on-axis heating and CNTR-CD deposition are too far from the center to allow a sufficient increase of the temperature profile. Correspondingly, the OH current is

not able to increase enough to compensate the strong negative effect of the CD and this produces a hole in the total current profile: the corresponding safety factor profile is not favourable for confinement in the RLW local transport model and this produces a loop in which the simulated temperature drops more and more. In Fig. 9 the simulated and

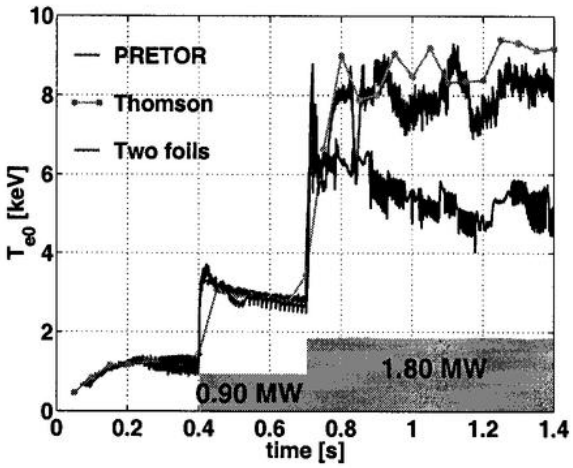

Fig. 7. *Simulated and measured T_e on-axis for shot ♯18639*

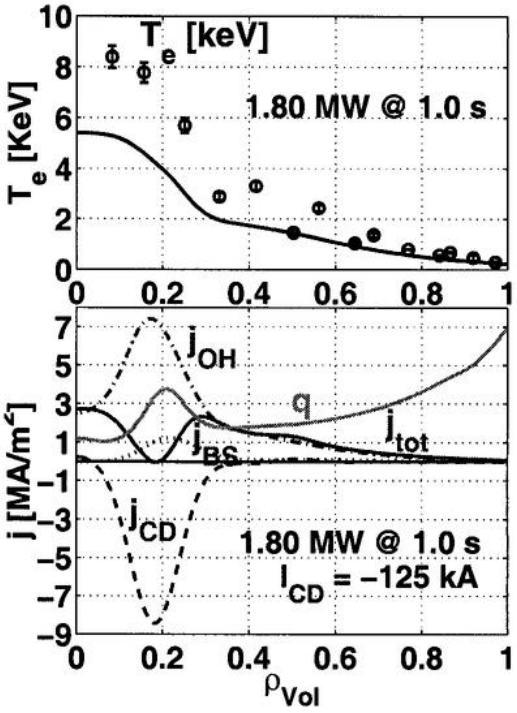

Fig. 8. *Simulated and measured T_e profile and simulated current densities and q profiles for shot ♯18639*

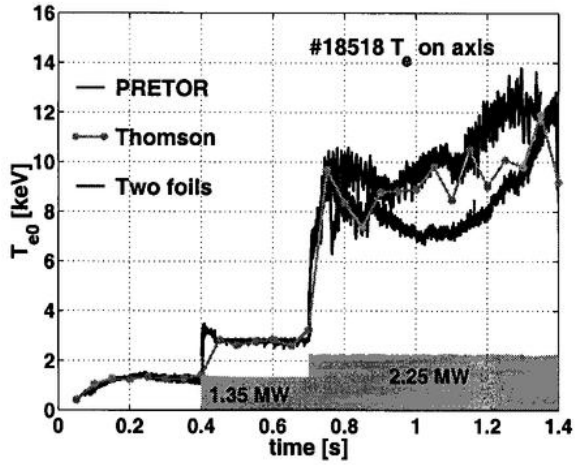

Fig. 9. *Simulated and measured T_e on-axis for shot ♯18518*

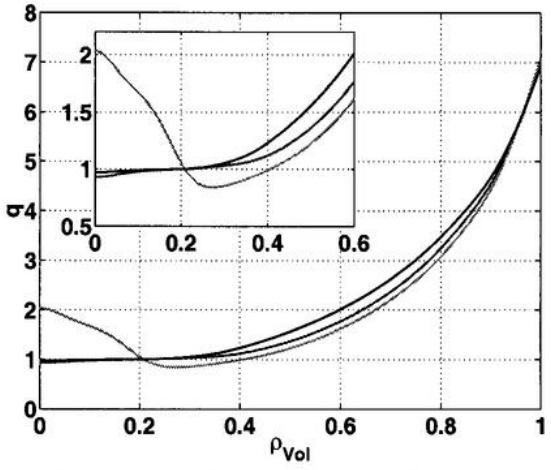

Fig. 10. *Safety factor profiles for ♯18518*

experimental central temperatures for shot ♯18518 are shown: a very good agreement is found. In this case, as shown by the safety factor profiles, Fig. 10, the central CNTR-CD produces a largely negative safety factor profile in the center, which results in a low transport coefficient in the center. The local χ_e with 2.25 MW injected power is at the same level as in Ohmic heating, Fig. 11, and in agreement with the experimental estimations of the transport coefficients obtained from the Thomson scattering profiles. The simulated temperature profiles are in good agreement with the experimental measurements in all the phases of the discharge, Fig. 12. The high sensitivity on the CNTR-CD density profile is

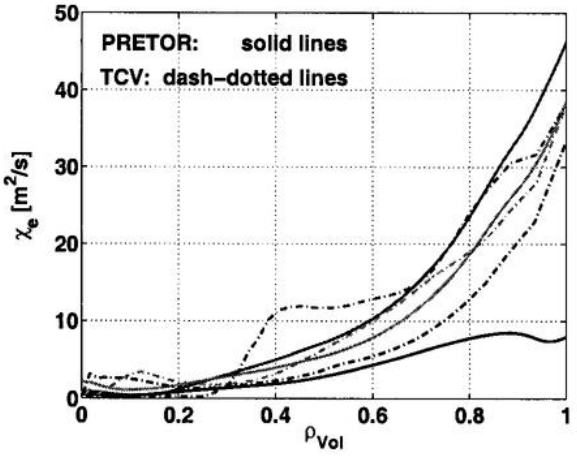

Fig. 11. χ_e *profiles for ♯18518*

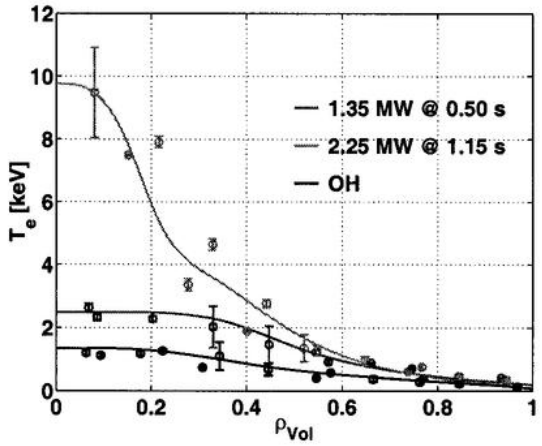

Fig. 12. T_e *profiles for ♯18518*

found also experimentally: several discharges have been produced on TCV, showing that very small alterations of the poloidal injection angle, corresponding to a distance less than the beam size (∼2 cm) in the central plasma region, cause important variations on the central temperature, of the order of 40%, and on the global confinement. A further more accurate investigation is needed, both experimental and theoretical, but, the absence of measurements of the current density or of the safety factor profile leaves too much degree of freedom to be stringent in the validation of a particular dependence of the transport model on the safety factor and current density profiles. However, these experimental results with CNTR-CD and the comparison with the the ECH case, shot ♯18604, allow us to conclude that the current profile tailoring plays the crucial role in obtaining the ICC regime. This alone indicates that the current density and safety factor profiles have a large influence on the electron transport coefficient. This is in agreement with the strong dependence on the safety factor profile found theoretically in all the principal underlying phenomena which can be relevant to electron anomalous transport: the turbulence in the magnetic topology [17], the trapped electron modes (TEM) coupled with the ion temperature gradient (ITG) modes [18] and the electron temperature gradient (ETG) modes [19].

3 Sawtooth period simulations of discharges with ECH poloidal sweeps

The TCV tokamak is a unique facility to explore the influence of ECH on the sawtooth activity: many types of central relaxation oscillations have been observed in various experiments [20], [21]. Small alterations of the ECH radius or seemingly negligible amounts of ECCD close to the q = 1 surface can strongly change the sawtooth period and shape. The sawtooth response to precise heating conditions is highly reproducible: in this sense sawteeth can be used as an ECH deposition detector [10]. When producing a poloidal sweep of the power deposition vertically along the minor radius, from the bottom to the top of the poloidal cross section, it is found experimentally that two specific locations maximize the sawtooth period: this gives a first precise test on the sawtooth crash model. In particular, as shown in Fig. 13, the first maximum is of lower amplitude and less localized, whereas the second one is of higher amplitude and highly localized. This comes from the geometrical configuration of the ECH launcher, which implies that, when heating at the bottom of the plasma, the deposition width is broader and a small amount of CNTR-CD is produced; whereas, when heating at the top, the deposition width is narrow

and accompanied by a small amount of CO-CD, Fig. 14. Both the beam width and the current drive affect the sawtooth period. Dedicated experiments have been performed

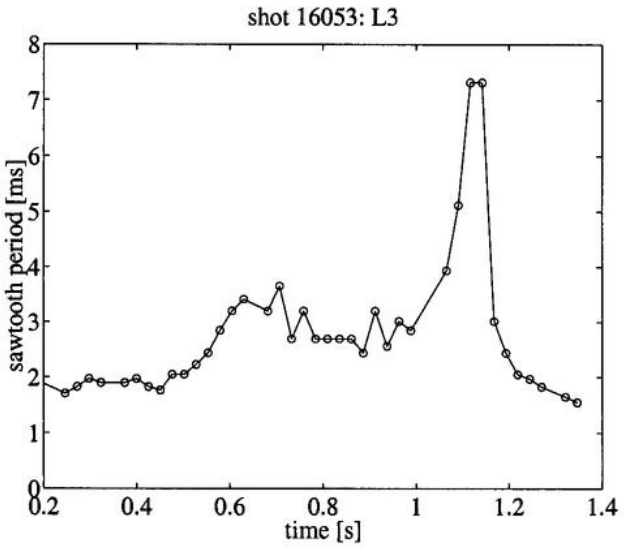

Fig. 13. *Experimental sawtooth period in ♯16053*

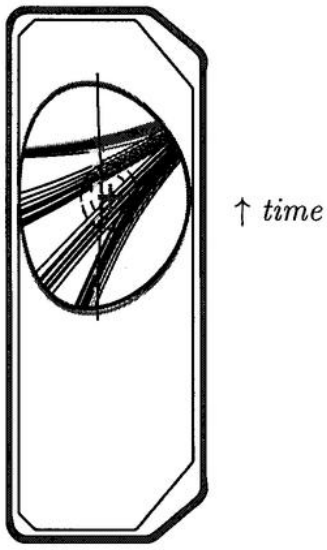

Fig. 14. *TORAY results poloidal view at 4 time slices during the sweep in ♯16053*

which have clearly confirmed these two effects [22]. First, the sawtooth period, at constant injected power, is sensitive to the deposition width, hence to the power density. Second, even negligible amounts of current drive, less than 1% of the plasma current, close to the q = 1 surface, can strongly change the sawtooth period. All these experimental findings give precise tests for the validation of a sawtooth crash model.

3.1 The sawtooth crash model

The sawtooth crash model used in these simulations is largely described in [9], and first proposed in [7]. Here, we reiterate the basic points of the model to more easily present what will follow. When the ideal internal kink is stable, and this is always the case in TCV for the discharges presented in this paper, the triggering condition for a crash is assumed to be given by

$$\gamma_\eta > c_* \ (\omega_{dia\,e}\ \omega_{dia\,i})^{1/2}\,, \tag{9}$$

that is, the crash is triggered when the resistive growth rate exceeds the stabilization given by diamagnetic effects on the q = 1 surface. Note that the diamagnetic frequencies enter the relevant dispersion relations in different ways, depending on the collisional regime and on whether the electrons are considered adiabatic or isothermal. The choice in Eq. 9, [9], close to the collisionless limit, is just the simplest possible expression. The coefficient c_* is a free parameter of the model, equal to 1 in the collisionless cylindrical limit. As the resistive growth rate depends on the magnetic shear, the condition can be inverted and rewritten in the form $s_1 > s_{1\,crit}$, where s_1 is the shear at q = 1, and the critical shear $s_{1\,crit}$ is a function of the local plasma parameters at q = 1; in particular it is nearly proportional to the pressure scale length. Simulating the sawtooth period over a wide range of different shots, it has been found that to fit the experimental sawtooth period the parameter c_* must be varied only between 0.5 and 1.5. When simulating the sawtooth period in a full ECH discharge, the parameter c_* is kept constant, and fitted to the sawtooth period in the ohmic phase of the discharge. After the crash the q profile is relaxed according to the Kadomtsev complete reconnection model. The temperature and

density profiles are flattened up to the mixing radius, while keeping the total particle and energy conserved.

3.2 Full poloidal sweep simulation: shot ♯16053

In the simulation of the sawtooth period for a discharge with a poloidal sweep, all the different effects presented above, in particular the variation of the deposition width and the small amounts of CD involved, must be carefully taken into account. This is possible by interpolating the ray-tracing results, calculated with TORAY every 50 ms. In Fig. 15 the sawtooth period evolution obtained in the simulation is presented. The main features of the experimental results are well reproduced by the model. In particular the presence

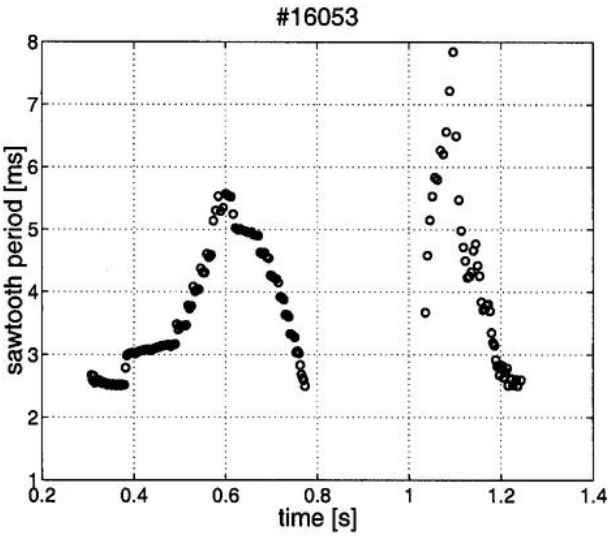

Fig. 15. *Simulated sawtooth period for ♯16053*

of two evident maxima, the first less localized with shorter sawtooth period, the second more localized with longer sawtooth period. Also the magnitude of the sawtooth period variations is in agreement with the experiment. From the simulation it is found that the deposition radius maximizing the sawtooth period is clearly outside the q = 1 surface, and even outside the mixing radius for broad deposition profiles; but, closer to the q = 1 surface with more localized power. Although some experimental evidence suggests that the deposition radius maximizing the sawtooth period is outside the experimental inversion radius, a conclusive validation needs accurate equilibrium reconstruction, with experimental constraints on the current profile, which are not available on TCV. Hence this prediction amounts to a further validation test for the model.

3.3 Sawtooth period and power density: shot ♯16487

A dedicated experiment has been performed in shot ♯16487 which has definitely confirmed the influence of the power density on the sawtooth period. The deposition radius maximizing the sawtooth period was identified in a previous discharge by sweeping two beams in the manner described above. Then two launchers were used to sweep across this position in opposite direction such as to keep the total power inside this flux surface constant, but modifying the power density at this position. The experimental result, together with the power deposition densities from TORAY at two time slices of the discharge are shown in Fig. 16 and 17 respectively. The power density at $\rho_{dep} = 0.37$ increases progressively between the two time slices presented, and the sawtooth period also, increasing from 12 ms up to almost 20 ms. Performing the same crossed sweep with PRETOR,

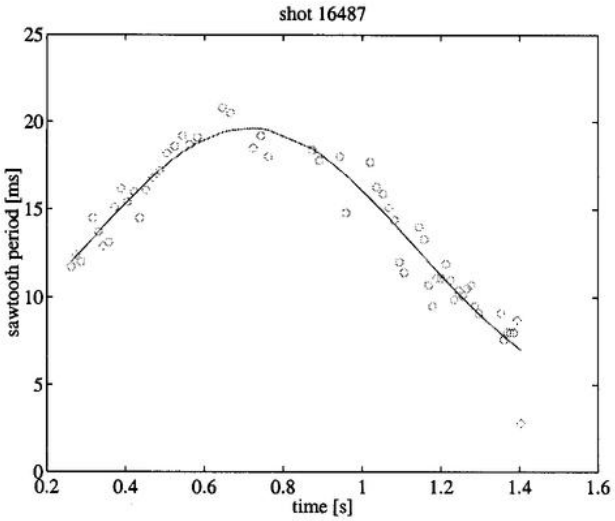

Fig. 16. *Experimental sawtooth period in ♯16487*

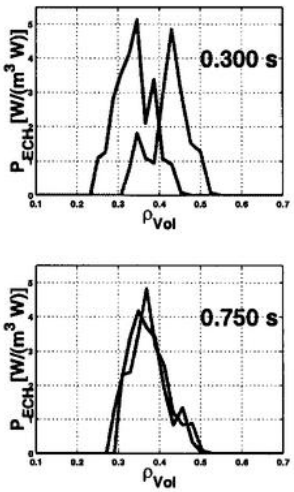

Fig. 17. *TORAY ECH deposition profiles at two time slices in ♯16487*

the sawtooth period variation of Fig. 18 has been found, completely consistent with the experimental results. Note that we had also first to identify the position maximizing the sawtooth period in the PRETOR simulation and have used this position as reference for the cross-sweep. This position is 0.43 in PRETOR, which is within the error bars on the temperature and density measurements, the TORAY deposition profiles, and perhaps most importantly the equilibrium reconstruction. Considering the crash criterion, two effects are produced by the larger power density, Fig. 19. First the shear after the crash increases more slowly, second the critical shear also increases because of the enhancement of the pressure scale length at q = 1 due to the more localized power deposition outside q = 1. Both these effects imply a longer sawtooth period and explain the experimental results.

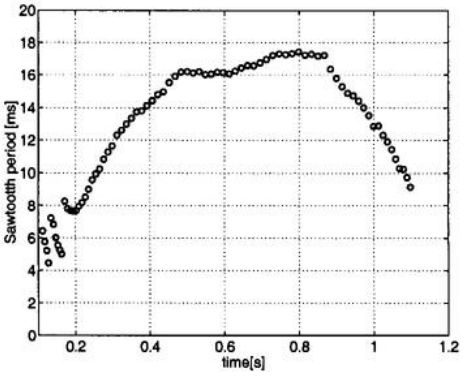

Fig. 18. *Simulated sawtooth period in ♯16487*

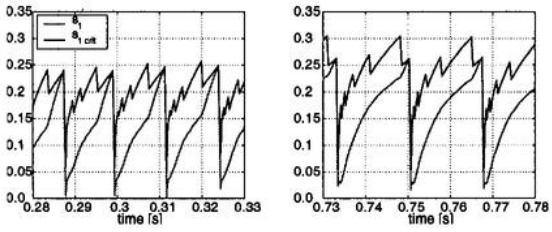

Fig. 19. *Shear at q = 1 and critical shear with sawtooth period of 11 ms (left) and sawtooth period of 18 ms (right)*

3.4 Sawtooth period and current drive

Two shots have been produced with identical plasma conditions, but in one case, shot ♯15278, the ECH power deposited close to the q = 1 surface is accompanied by a small amount (less than 1% of the total current) of CNTR-CD, in the other case, shot ♯15282, the same power deposition is accompanied by a similar amount of CO-CD [22]. The sawtooth period turns out to be strongly sensitive to this negligible inversion of current

drive. This variation is well reproduced by the model. In Fig. 20 the results of the simulation are shown. When changing the amount of current drive from -2.8 to +2.8 kA,

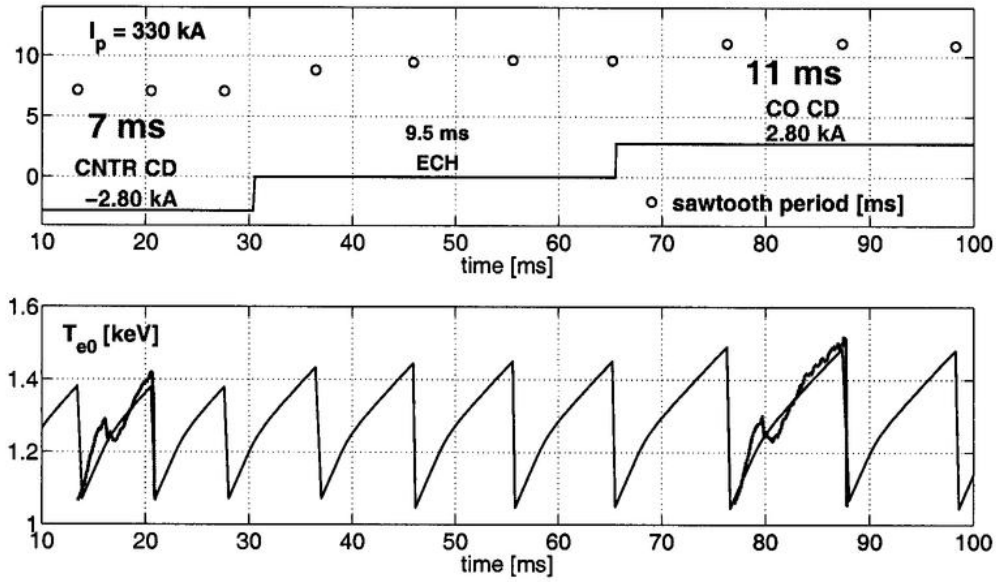

Fig. 20. *Sawtooth period variation (above) and central T_e for shots ♯15278 and ♯15282*

with a plasma current of 330 kA, the simulated sawtooth period changes from 7 ms to 11 ms, completely in agreement with the experimental results, as shown by the simulated central electron temperature trace, on which two experimental sawtooth periods from the soft X-ray traces of the two shots, rescaled in amplitude, have been plotted. In this case, as the ECH power deposition is the same in the two shots, the critical shear behaviour does not change in the two situations, remaining constant at the trigger. On the contrary, the small amount of CD, localized close to the q = 1 surface, changes the dynamics of the shear at q = 1, which, after the crash, increases more quickly with the CNTR-CD contribution, and more slowly with CO-CD. This is sufficient to alterate the time at which the crash condition is triggered, changing the sawtooth period from 7 ms up to 11 ms.

4 Conclusions

The interface implemented between PRETOR and TCV allows the code to be used as a complete TCV simulator and predictor. The self-consistent evolution of a 2D equilibrium during the simulation is essential in order to accurately describe the influence of ECH/ECCD on the current density and safety factor profiles.

With only ECH, confinement largely exceeding the global RLW scaling law is obtained. Power localization in low transport plasma region explains these results: the RLW local transport model allows simulations in very good agreement. Note that this effect is favourable for reactor scenario where the deuterium heating source is expected to be localized in the center. With strong on-axis CNTR-CD, the current density profile tailoring plays a crucial role in the Improved Central Confinement regime, characterized by H_{RLW} factors up to 3.5. Negative shear scenarios are likely to be obtained. In the simulation of the ICC discharges, the high sensitivity of the safety factor profile on the ECH/ECCD deposition profile does not allow a conclusive validation of the transport model. However some numerical results in very good agreement with experiments have been found. This sensitivity has been confirmed by preliminary experimental results and should allow further experiments to determine whether with high central electron temperature gradients,

the electron transport is reduced only in the case of negative shear profiles, as the local RLW model used in the simulation would suggest, or also by more flat safety factor profiles.

A sawtooth crash model based on a critical shear value at q = 1 is in agreement with very detailed experimental results obtained with different ECH configurations. In particular the strong sensitivity of the sawtooth period on very small alteration of the power deposition or on very small amounts of current drive near the q = 1 surface are well reproduced by the model: the presence of two locations maximizing the sawtooth period in a full poloidal sweep are in complete agreement with the experimental results. The identification of these locations with respect to the safety factor profile is a further validation test for the model, but will require more accurate equilibrium reconstruction.

Acknowledgments

This work was supported in part by the Swiss National Science Foundation.

References

[1] D. Boucher *et al*, in Proc. IAEA Tech. Com on Advances in Simulation and modell. of Thermonuclear plasmas, 1992, Montreal (1993), p. 142.
[2] T. P. Goodman *et al*, Proc. 19th SOFT, Lisbon (1996), p. 565.
[3] F. Hofmann *et al*, Plasma Phys. Contr. Fusion **36**, B277 (1994).
[4] G. R. Smith *et al*, in Proc. 9th Joint Workshop on ECE and ECRH, Borrego Springs, California (January 1995), Editor World Scientific (1995) p. 651.
[5] Z.A. Pietrzyk, C. Angioni *et al*, Proc. of 27th EPS Conf. on Contr. Fusion and Plasma Physics, Budapest, 2000, paper P4.099.
[6] P.H. Rebut, P.P. Lallia and M.L. Watkins, Proc. 12th Int. Conf. Plasma Physics and Controlled Nuclear Fusion Research, Nice 1988, IAEA Vienna 1989, Vol. 2, p. 191.
[7] F. Porcelli *et al*, Plasma Phys. Contr. Fusion **38**, 2163 (1996).
[8] C. Angioni *et al*, in *Theory of Fusion Plasmas*, Proc. Joint Varenna-Lausanne International Workshop, Varenna, 1998 (J.W. Connor, E. Sindoni, J. Vaclavik, Eds), ISSP-18, Editrice Compositori, Bologna (1999), p. 493.
[9] O. Sauter *et al*, *ibidem* [8], p. 403.
[10] T. P. Goodman *et al*, Proc. of 26th EPS Conf. on Contr. Fusion and Plasma Physics, Maastricht, 1999, ECA Vol.23J (1999) p. 1101.
[11] G. Bateman *et al*, Phys. Plasmas **5**, 1793 (1998).
[12] M. Kotschenreuter *et al*, Phys. Plasmas **2**, 2381 (1995).
[13] I. Furno, H. Weisen, Proc. of 27th EPS Conf. on Contr. Fusion and Plasma Physics, Budapest, 2000, paper P1.026.
[14] R. Behn *et al*, Proc. of 26th EPS Conf. on Contr. Fusion and Plasma Physics, Maastricht, 1999, ECA Vol.23J (1999) p. 1065.
[15] F. Hofmann, Tonetti G., Nucl. Fusion **28**, 1871 (1988)
[16] O. Sauter, C. Angioni, and Y.R. Lin-Liu, Phys. Plasmas **6**, 2834 (1999).
[17] P.H. Rebut, M. Hugon, Proc. 10th Int. Conf. Plasma Physics and Controlled Nuclear Fusion Research, London 1984, IAEA Vienna 1985, Vol. 2, p. 197.
[18] S. Brunner, M. Fivaz, T.M. Tran, and J. Vaclavik, Phys. Plasmas **5**, 3929 (1998).
[19] F. Jenko, *et al* Phys. Plasmas **7**, 1904 (2000).
[20] A. Pietrzyk *et al*, Nucl. Fusion **39**, 587 (1999).
[21] I. Furno, C. Angioni, F. Porcelli, H. Weisen, *et al*, accepted for publication in Nucl. Fusion.
[22] M.A. Henderson, T.P. Goodman, *et al*, in Proc. of Int. Workshop on *Strong Microvaves in Plasmas*, Nizhny Nogvorod 1999, edited by A.G. Litvak (2000), p. 114;
M.A. Henderson, *et al*, to be published in Fusion Engineering and Design.

Global Linear Gyrokinetic PIC Simulations in 3D Magnetic Configurations

G. Jost, T.M. Tran, K. Appert, W.A. Cooper, L. Villard

Centre de Recherches en Physique des Plasmas
Association Euratom - Confédération Suisse
Ecole Polytechnique Fédérale de Lausanne

1 Introduction

It is now commonly accepted that the turbulence resulting from the nonlinear saturation of microinstabilities, particularly Ion Temperature Gradient (ITG) driven modes, plays an important role in the anomalous transport observed in tokamaks. However, in contrast with tokamaks, there is no experimental evidence of anomalous transport in the plasma core in stellarators. Transport in these devices is currently well explained with the help of the neoclassical theory except near the edge of the configurations where turbulence occurs [1]. This explains the small number of theoretical studies on anomalous transport in these devices [2, 3, 4, 5, 6, 7, 8]. Futhermore, the next generation of stellarators, particularly the quasi-symmetric (QS) systems [9], are hoped to be characterized by a much smaller neo-classical transport and by particle confinement close to that of tokamaks. There is then a strong interest in the stellarator community to study the properties of drift waves in 3D magnetic configurations.

To serve this interest we have developed the first global gyrokinetic code EUTERPE [10, 11], aimed at the investigation of linear drift wave stability in general toroidal equilibria with nested magnetic surfaces provided by the VMEC code [12]. Indeed, it should be noted that all the above mentioned works reduce a full 3D problem to a one-dimensional problem where the potential is computed only along one magnetic field line. With such a local model each magnetic field line is independent, the coupling between magnetic surfaces and the coupling between magnetic field lines along a given magnetic surface are neglected. In other words, this model does not treat perpendicular propagation fully adequately. Also as pointed out by Kendl [7], finding the most unstable mode with such a model is very expensive, because a large number of magnetic field lines need to be taken into account in order to cover completely the configuration. Only with a global approach can such a problem be solved in a straightforward and transparent way.

We present here the first global gyrokinetic linear study of ITG driven modes for two realistic 3D configurations, namely the Quasi-Axially symmetric Stellarator with three fields periods (QAS3) [13] and the Helically Symmetric eXperiment (HSX) [14]. Both are 3D configurations characterized by a quasi-symmetric magnetic field. In both configurations, we have investigated the effects of the 3D shape on the linear stability of the ITG driven mode. We have then developed a sequence of configurations which vary from the quasi-symmetric systems to the corresponding symmetric ones.

2 Physical model and numerical implementation

For a 3D static equilibrium with nested magnetic surfaces, i.e. the magnetic fluxes are only function of the normalized radial variable s, the equilibrium magnetic field $\vec{B}$ can be written in contravariant form as follows [12] :

$$\vec{B} = \vec{\nabla}\varphi \times \vec{\nabla}\chi(s) + \vec{\nabla}\Phi(s) \times \vec{\nabla}\theta^*, \tag{1}$$

where $2\pi\chi(s)$ and $2\pi\Phi(s)$ are respectively the poloidal and toroidal fluxes enclosed between the magnetic axis ($s = 0$ where $\vec{\nabla}\chi = 0$) and the magnetic surface labeled s. φ is the geometric toroidal angle and θ^* the poloidal angle which makes the magnetic field lines straight. We can define the normalized radial variable s as $s = \Phi/\Phi_0$ where $2\pi\Phi_0$ is the value of the toroidal flux at the edge of the plasma (at $s = 1$). The coordinates (s, θ^*, φ) define the PEST-1 system of magnetic coordinates [15].

The plasma is modeled by gyrokinetic ions and adiabatic electrons, and we follow the linear time evolution of quasi-neutral electrostatic perturbations of the local Maxwellian distribution function in a 3D magnetic configuration. We assume a collisionless neutral static plasma where the equilibrium ion density n_0 is equal to the electron density, T_i and T_e are the equilibrium ion and electron temperature, respectively, and the thermal velocity of the ions is given by $v_{thi} = \sqrt{T_i/m_i}$ where m_i is the ion mass. The ion cyclotron frequency is given by $\Omega = q_i B/m_i$, where q_i is the ion charge. In such a plasma, particles are freely streaming along the magnetic field lines and we assume that the plasma is homogeneous along the magnetic field lines, i.e. $\vec{B} \cdot \vec{\nabla} T_{\{i,e\}} = 0$ and $\vec{B} \cdot \vec{\nabla} n_0 = 0$.

Within the gyrokinetic model and neglecting pressure effects, the equations for the particle guiding centers are given by [16, 17] :

$$\frac{d\vec{R}}{dt} = v_\parallel \vec{h} + \frac{v_\parallel^2 + v_\perp^2/2}{\Omega} \vec{h} \times \frac{\vec{\nabla} B}{B}, \tag{2}$$

$$\frac{dv_\parallel}{dt} = \frac{1}{2} v_\perp^2 \vec{\nabla} \cdot \vec{h}, \tag{3}$$

$$\frac{d\mu}{dt} = 0, \tag{4}$$

where $\vec{R}$, $v_{||}$ and μ denote the position, the parallel component of the velocity of the guiding center and the first adiabatic invariant $\mu = v_\perp^2/2B$, respectively. Here, $v_\perp$ is the perpendicular component of the velocity. The position $\vec{R}$ of the guiding center is related to the particle position $\vec{x}$ by : $\vec{x} = \vec{R} + \vec{v} \times \vec{h}/\Omega$.

The perturbed part f of the ion distribution function evolves linearly according to :

$$\begin{aligned} \frac{d}{dt} f(\vec{R}, v_{||}, \mu, t) &= -\frac{\langle \vec{E} \rangle \times \vec{B}}{B^2} \frac{\partial f_0}{\partial \vec{R}} - \frac{q_i}{m_i} \vec{h} \cdot \langle \vec{E} \rangle \frac{\partial f_0}{\partial v_{||}} \\ &\quad - \left(v_{||} \frac{\partial f_0}{\partial v_{||}} + \frac{1}{2} v_\perp \frac{\partial f_0}{\partial v_\perp} \right) \langle \vec{E} \rangle \cdot \vec{h} \times \frac{\vec{\nabla} B}{B^2}, \end{aligned} \tag{5}$$

where $\langle \vec{E} \rangle$ denotes the gyro-averaged electric field. In the limit $(k_\perp \rho)^2 \ll 1$, the perturbed ion density n_i becomes [17]:

$$n_i(\vec{x}, t) = \int f(\vec{R}, v_{||}, \mu, t) \delta^3(\vec{R} - \vec{x} + \vec{\rho}) B d\vec{R} d\alpha dv_{||} d\mu + \vec{\nabla}_\perp \cdot \left[\frac{n_0}{B\Omega} \vec{\nabla}_\perp \phi \right]. \tag{6}$$

where ϕ, ρ and α are the electrostatic potential, the Larmor radius and the gyro-angle, respectively. Note that the gyro-averaged electric field in eq. (5) is given by $\langle \vec{E} \rangle = -\vec{\nabla} \langle \phi \rangle$ where $\langle \phi \rangle$ is the gyroaveraged potential :

$$\langle \phi \rangle (\vec{R}, v_{||}, \mu, t) = \frac{1}{2\pi} \int_0^{2\pi} d\alpha \phi(\vec{x}, t)(\vec{R} - \vec{x} + \vec{\rho}). \tag{7}$$

Assuming the electron response to be adiabatic, the system of equations is closed invoking quasi-neutrality and the Poisson equation reads :

$$\frac{e n_0}{T_e} \phi - \vec{\nabla}_\perp \cdot \left[\frac{n_0}{B\Omega} \vec{\nabla}_\perp \phi \right] = \int f(\vec{R}, v_{||}, v_\perp, t) \delta^3(\vec{R} - \vec{x} + \vec{\rho}) B d\vec{R} d\alpha dv_{||} d\mu. \tag{8}$$

The equations governing the ions (2-5) and the above Poisson equation (8) coupled with equation (7) constitute the final system of equations of our model.

In contrast with axisymmetric configurations, in a 3D geometry the equations of motion of the guiding centers do not conserve an additional integral of motion, like the toroidal canonical angular momentum in a tokamak [17]. Here, the equilibrium ion distribution function f_0 must be chosen following other criteria. Using the conditions $\vec{B} \cdot \vec{\nabla} T_i = 0$ and $\vec{B} \cdot \vec{\nabla} n_0 = 0$, we choose f_0 as a local Maxwellian,

$$f_0(v_{||}, v_\perp, s) = \frac{n_0(s)}{(2\pi)^{3/2} v_{thi}^3(s)} \exp\left(-\frac{1}{2} \frac{v_{||}^2 + v_\perp^2}{v_{thi}^2(s)} \right). \tag{9}$$

The linearized 3D gyrokinetic equations (2-5,7,8) are solved numerically using an improved version of the PIC method, the so-called δf method [18] and the 3D

gyrokinetic Poisson equation (8) is solved in the PEST-1 system of coordinates using finite elements, details are given in ref. [10].

Furthermore, this system of equations is solved with the help of the extraction of the ballooning phase factor [17]. In a 3D configuration, the global ITG driven mode is characterized by several poloidal and toroidal wavenumbers. However, the condition $k_{||} \approx 0$ implies that the dominant poloidal wavenumber m_0 is related to the dominant toroidal wavenumber n_0 by $m_0 \approx -n_0 q$. Following [17], we can rewrite the electrostatic potential as :

$$\phi(s, \theta^*, \varphi, t) = Re\left(\tilde{\phi}(s, \theta^*, \varphi, t) e^{iS(\theta^*, \varphi)}\right), \tag{10}$$

where $\tilde{\phi}$ is the extracted potential and S the ballooning phase factor is given by :

$$S(\theta^*, \varphi) = m_0 \theta^* + n_0 \varphi. \tag{11}$$

Here, m_0 and n_0 are integer numbers which are both input parameters of the code, the ballooning phase S and the extracted electrostatic potential $\tilde{\phi}$ are then periodic functions of θ^* and φ. Usually, we choose $m_0 \approx -n_0 q(s_0)$, with $q(s_0)$ the safety factor at $s = s_0$ where the ion temperature gradient peaks. As we solve only the slow spatial variation $\tilde{\phi}$ of the potential, the total number of grid points and particles is almost independent of the poloidal and toroidal wavenumbers m_0 and n_0.

Lastly, the right-hand side of the discretized Poisson equation (eq. 6) is Fourier filtered in the poloidal and toroidal directions [17, 18]. Generally, we only keep the poloidal and toroidal harmonics characterized by low values of $k_{||}$ and, as we have seen in sec. 3, the harmonics resulting from the coupling induced by the magnetic field, the shape and width of the Fourier filter being a function of the configuration.

3 Effects of a 3D magnetic field on the ITG driven mode

In tokamaks, global results [19, 17] have shown that the toroidal ITG is characterized by several poloidal wave numbers m centered around nq, with q the value of the safety factor where the toroidal ITG is peaking, the most unstable mode being characterized by $k_{||} \approx 0$. The coupling between the different poloidal wave numbers m is resulting from the spatial structure of B along a magnetic surface. In a simple geometry, a circular large aspect ratio tokamak, it is given in first approximation by [19] :

$$\frac{1}{B(r,\theta)} \approx \frac{1}{B(r)}\left(1 + \frac{r}{R_0}\cos(\theta)\right). \tag{12}$$

Particularly, the $\cos(\theta)$ term creates a $(m, m+1)$ coupling between the different poloidal components, i.e. it creates a coupling between the poloidal wavenumbers m and $m+1$.

We can try to extrapolate these results obtained in a very simple 2D configuration to the 3D systems. In such systems, obviously, the modulus of the magnetic field B is a function of the 3 coordinates (s, θ^*, φ). The spectrum of B provides us information about the expected couplings in a 3D system. Considering a magnetic field $B = \sum_{m',n'} B_{m',n'}(s)\cos(m'\theta^* + n'\varphi)$, we assume that the amplitude of the $B_{m',n'}(s)$ coefficients is related to the intensity of the coupling between the (m,n) and the $(m+m', n+n')$ components of the ITG driven mode. We will denote this coupling $((m,n),(m+m',n+n'))$.

In a preliminary study [11] performed in a tokamak perturbed by a L=2 helical boundary deformation with $N_{per} = 4$ numbers of field periods, we have been able to validate this assumption. In this configuration, the spectrum of B is dominated by the $B_{1,0}$, $B_{2,2N_{per}}$ and $B_{1,2N_{per}}$ Fourier coefficients, the $B_{1,0}$ coefficient is characteristic of a tokamak. We then obtained a 3D ITG driven mode characterized by several toroidal modes numbers satisfying $\mathrm{mod}(n-n', 2N_{per}) = 0$. However, it should be noted that the coupling resulting from the helical deformation was weak compared with the coupling induced by the toroidal effects, i.e. the effects of the $B_{1,0}$ Fourier harmonic. The amplitudes of the couplings $((m,n),(m+m',n+n'))$ are not directly proportional to the amplitudes of the $B_{m',n'}(s)$ coefficients.

4 Results

We present here the results obtained by EUTERPE in both realistic configurations, QAS3 and HSX. Note that during all our studies, the pressure effects are neglected, $\beta = 0$, the equilibrium ion density n_0 and the electron temperature $T_e(s) = T_i(s_0)$ are constant. The equilibrium ion density n_0 is constant and we choose the equilibrium ion temperature T_i :

$$\frac{1}{T_i}\frac{dT_i}{ds_\chi} = -\kappa_T \cosh^{-2}\left(\frac{s_\chi - s_{\chi 0}}{\Delta s_\chi}\right), \tag{13}$$

where s_χ is a normalized radial variable defined with the poloidal flux $s_\chi = \sqrt{\chi/\chi_0}$, $2\pi\chi_0$ is the poloidal flux at the edge of the plasma.

We first investigate the global linear stability of the ITG driven mode in the realistic QAS3 configuration [13]. Note that in contrast with the 3D quasi-axisymmetric configurations [20] which are characterized by a magnetic field similar to those of a tokamak, i.e. a spectrum of B dominated by the $B_{1,0}$ component, the magnetic structure of QAS3 shown in Fig. 2 has also a strong $B_{0,1\times N_{per}}$ component, the so-called

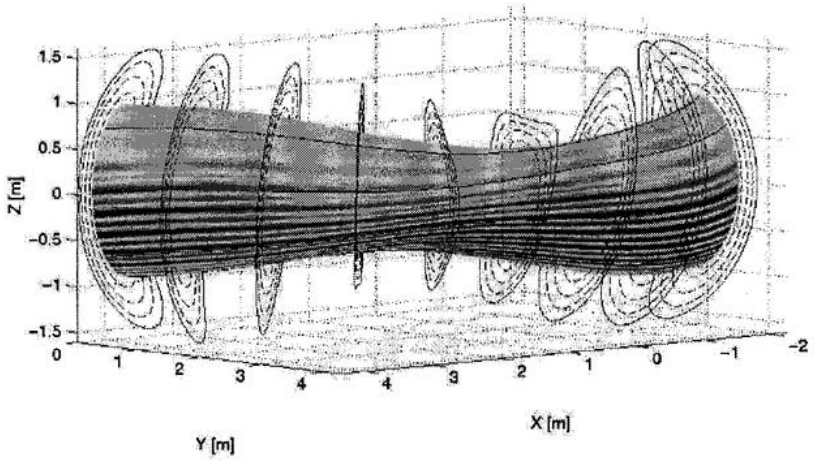

Figure 1: *Contour of the electrostatic potential over one period of QAS3. We show here the mode* $m_0 = -24, n_0 = 8$ *at* $s = s_0$. *Some magnetic surfaces intersections with poloidal planes (dashed lines) and some magnetic field lines (continuous lines) are also represented.*

mirror field component. For this spectrum, we define the following filter :

$$(m_i, n_j) = (m_0 + i, n_0 - jN_{per}), i = [-6, 6], j = [-4, 4], \tag{14}$$

where (m_i, n_j) denote the toroidal and poloidal wavenumbers kept during the simulations and N_{per} is the number of field periods, $N_{per} = 3$. Figure 2 shows also that QAS3 has negative shear $\hat{s}$. We choose an ion temperature gradient peaking at $s_0 = 0.34$ where $q(s_0) \approx 3$, $\kappa_T = 5$, $\Delta s_\chi = 0.21$, $\hat{s}(s_0) = -0.43$ and $\rho(s_0) = 1\text{cm}$.

With the above parameters, the dispersion relation computed by EUTERPE over one period of the configuration is represented in Fig. 3. Here, the maximum growth rate is not obtained with $n = 8$ where $k_\perp \rho \approx 0.5$, but with $n = 12$. This effect is due to the negative shear of the configuration and has already been observed in tokamaks [19]. Furthermore, Fig. 1 shows that the ITG driven mode is ballooning along all the torus in the outer part of the configuration, the so-called region of unfavorable curvature region. In this region, the amplitude of the magnetic field is only slightly varying along the toroidal direction. Here, the coupling resulting from the $B_{0,1\times N_{per}}$ Fourier harmonic is weak compared with the coupling induced by the toroidal effects, i.e. the effects of the $B_{1,0}$ Fourier harmonic. Therefore, this mode is almost characterized by only one toroidal wavenumber as in a tokamak. We have also verified that the most unstable mode $n = 12$ was not affected by trapped particles.

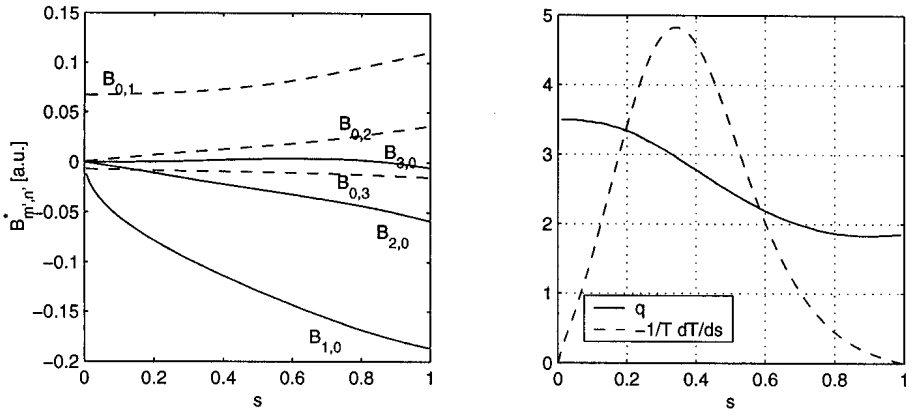

Figure 2: *Amplitude of the largest Fourier harmonics $B_{m',n'}$ as a function of s ($B_{0,0}$ is omitted) for QAS3 (left) and the safety factor q and the ion temperature profile as function of s (right).*

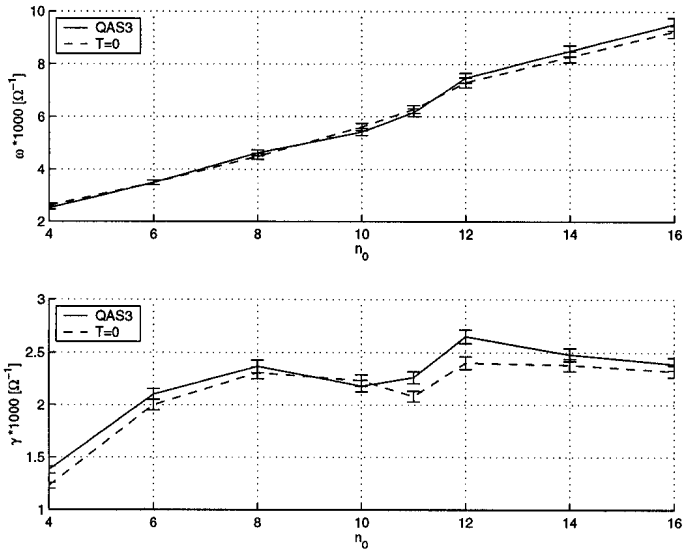

Figure 3: *Frequency and growth rate of the ITG driven mode measured in QAS3 and the equivalent tokamak ($T = 0$) as function of n_0.*

In our case, the modes obtained with and without the mirror term (eq. 3) in the equations of motion are identical, the frequency and the growth rate are not affected by trapped ions.

In QAS3, the properties of the ITG driven mode seem then to be very similar to those obtained in a tokamak. These results agree qualitatively with the local linear kinetic results obtained by Rewoldt [8].

To validate this feature of QAS3, we develop a sequence of configurations obtained by linearly varying the nonaxisymmetric Fourier coefficients of the surface of the

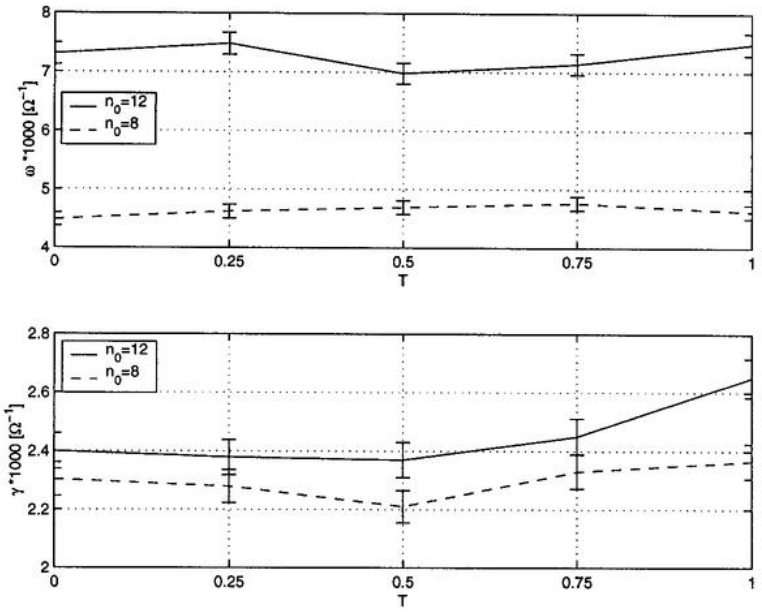

Figure 4: *Frequency and growth rate of the ITG driven modes* $n_0 = 12$ *and* $n_0 = 8$ *measured as function of* T.

plasma [21] :

$$
\begin{aligned}
R_T(s=1) &= \sum_{m',n'=0} R_{m',n'}(s=1)\cos(m'\theta - N_{per}n'v) + \\
&\quad T \sum_{m',n'\neq 0} R_{m',n'}(s=1)\cos(m'\theta - N_{per}n'v) \\
Z_T(s=1) &= \sum_{m',n'=0} Z_{m',n'}(s=1)\sin(m'\theta - N_{per}n'v) + \\
&\quad T \sum_{m',n'\neq 0} Z_{m',n'}(s=1)\sin(m'\theta - N_{per}n'v)
\end{aligned}
$$

where $R_{m',n'}(s=1)$ and $Z_{m',n'}(s=1)$ are the Fourier coefficients describing the edge of QAS3, T is a scalar. When $T = 0$, we obtain a pure axisymmetric configuration, the so-called equivalent tokamak. For all the configurations, we fix the safety factor profile (Fig. 2) and we almost keep the same number of Larmor radii along the s-axis by adjusting the value of the ion temperature at $s = s_0$.

The dispersion relation measured in the equivalent tokamak is also represented in Fig. 3, the frequencies and growth rates are very close to the values measured in QAS3. In Figure 4, the frequencies and growth rates of the modes $n = 8$ and $n = 12$ are plotted as a function of $T = (0., 0.25, 0.5, 0.75, 1)$. It shows that for both modes the frequency and growth rate are only slightly affected by the variation of the shape of the plasma. Here again, as shown in Fig. 5, the ITG driven mode $n = 8$ is ballooning around the torus in the outer part of all the configurations. The main

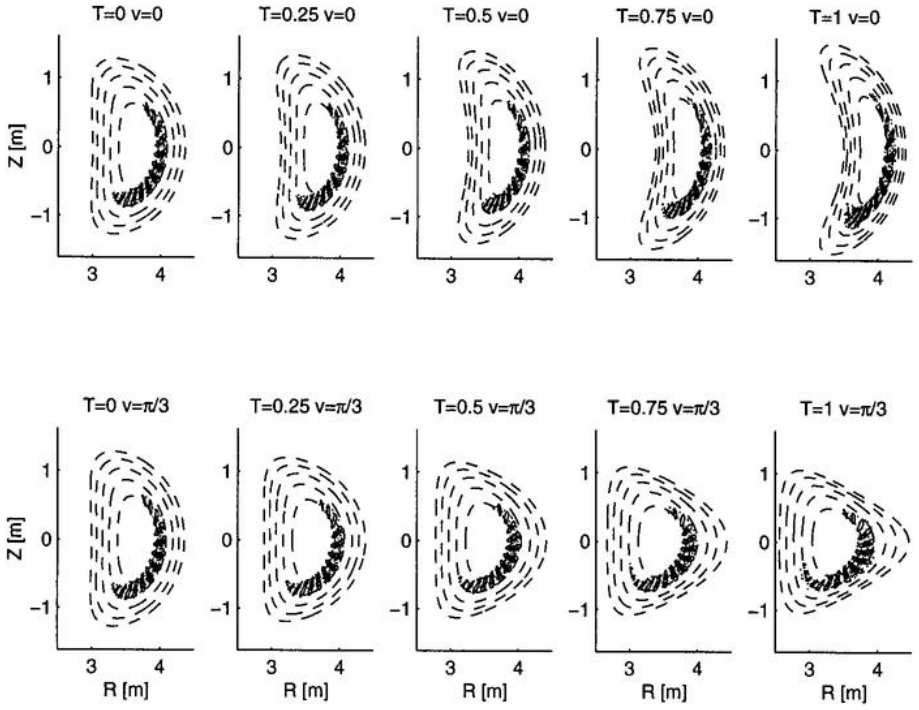

Figure 5: *Level surfaces of the electrostatic potential ϕ measured at $\varphi = 0$ (top) and $\pi/3$ (bottom) as a function of T with $m_0 = -24$ and $n_0 = 8$.*

properties of the ITG driven mode in QAS3 are governed by the global magnetic shear $\hat{s}$ of the configuration.

The HSX device shown in Fig. 6 is a helical axis stellarator with 4 field periods with quasi-helical symmetry. The spectrum of the magnetic field in HSX is dominated by the $B_{1,1\times N_{per}}$ Fourier coefficient, $B \approx B(s, \theta^* - N_{per}\varphi)$. The rotational transform is mainly provided by the helical magnetic field and is rather flat, $q(s = 1)/q(s = 0) \approx 0.95$.

The ion temperature gradient peaks in the middle of the configuration, at $s_0 = 0.25$ where $q(s_0) = 0.96$ and $\rho(s_0) = 0.21\text{cm} \approx \langle a \rangle/71$, where $\langle a \rangle$ is the averaged minor radius of the configuration. We choose $\Delta s_\chi = 0.21$ and $\kappa_T = 5$. Due to the strong helical symmetry of the magnetic field, we keep only the following poloidal and toroidal wavenumbers :

$$(m_i, n_j) = (m_0 + i, n_0 - iN_{per}), i = [-6, 6].$$

Figure 7 shows the mode $(m_0, n_0) = (-9, 8)$ obtained by EUTERPE with these parameters over one period of the configuration. In contrast with QAS3, the structure of the ITG driven mode is here characterized by a strong toroidal variation $|\max(\phi(\varphi = \pi/N_{per}))|/|\max(\phi(\varphi = 0))| \approx 1.5$. This property of the mode does not seem to be related to the magnetic structure of HSX and neither to the trapped ion

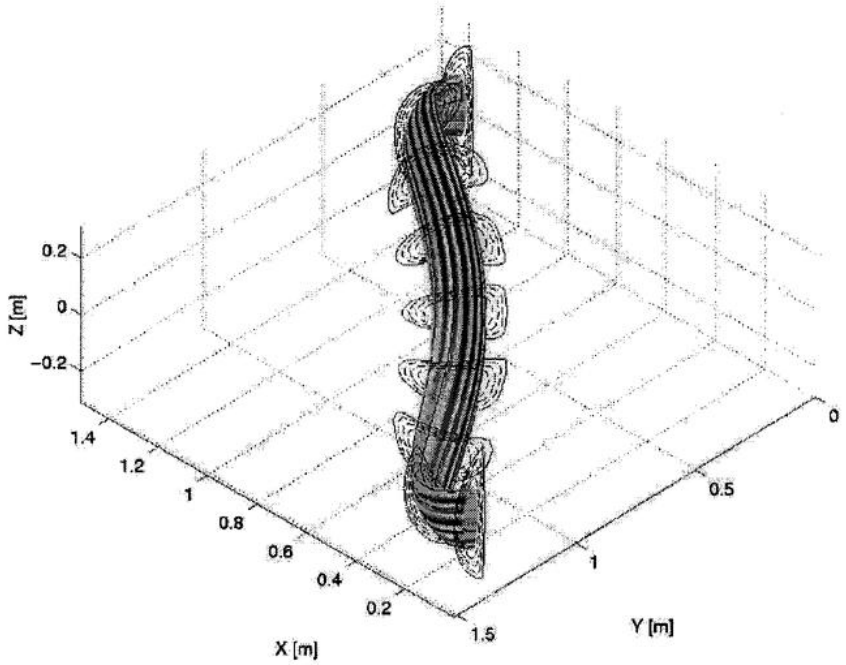

Figure 6: *Same as in Fig. 1, but in HSX. We show here the node* $m_0 = -9, n_0 = 8$ *at* $s = s_0$.

effects. Indeed, we obtain a similar toroidal variation of the mode by keeping only the m_0 and n_0 wavenumbers, the couplings induced by the magnetic field being then forbidden. Similarly, results are identical without the mirror term (eq. 3) in the equations of motion of the particles.

In order to understand this feature of HSX, we study the influence of the shape of the plasma by varying the configuration from a quasi-helically to a helically symmetric system. This transformation is achieved by increasing the number of field periods N, while the aspect ratio per period is kept constant [22]. The Fourier components of the plasma surface of the final helically symmetric configuration are such that :

$$\begin{aligned} Z^f_{m,m-1} &= R^f_{m,m-1}, \\ Z^f_{m,m+1} &= -R^f_{m,m+1}. \end{aligned}$$

Here, we choose the following transformation :

$$\begin{aligned} R_{m,n} &= \frac{R^f_{m,n} - R^{HSX}_{m,n}}{N^f_{per} - N^{HSX}_{per}} \left(N - N^{HSX}_{per}\right) + R^f_{m,n}, \\ Z_{m,n} &= \frac{Z^f_{m,n} - Z^{HSX}_{m,n}}{N^f_{per} - N^{HSX}_{per}} \left(N - N^{HSX}_{per}\right) + Z^f_{m,n}, \\ R_{0,0}/N &= R^{HSX}_{0,0}/N^{HSX}_{per}, \end{aligned}$$

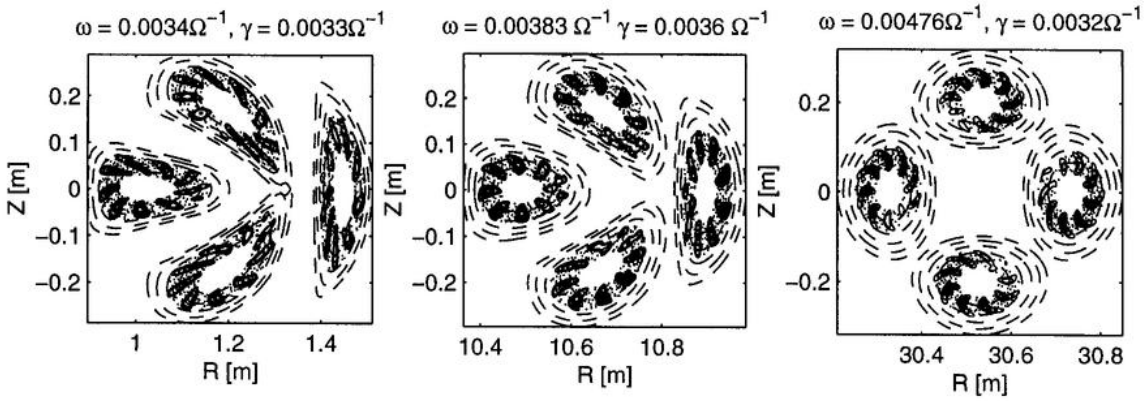

Figure 7: *Level surfaces of the electrostatic potential ϕ for HSX (left), $N = 35$ (center) and $N = 100$ (right). For each configuration, we show the mode at $\varphi = 0$ (right), $\pi/2N_{per}$ (top), π/N_{per} (left) and $3\pi/2N_{per}$ (bottom).*

where $N_{per}^{f} = 100$ is the number of field periods of the final configuration and the superscript ^{HSX} denotes the parameters describing the plasma surface of the HSX configuration. However, the q profiles vary during the transformation, we then have to adjust the values of n_0 to keep $k_{||}$ constant from a configuration to another one.

Figure 7 shows also the shape on the ITG driven modes with $N = 35$ and $N = 100$. Note that we obtain a helical-ITG mode when $N = 100$. The growth rate is almost constant while the frequency is an increasing function of N. Here again, these results were obtained by keeping the same number of Larmor radii between $s = 0$ and $s = 1$.

In Figs. 8 and 9, we plot the modulus of the extracted potential $\tilde{\phi}$ along the magnetic surface s_0 and compare its shape with those of the amplitude of the magnetic field and the Jacobian $\sqrt{g}^*$. When $N = 100$, the helical symmetry of the configuration is very well preserved by the EUTERPE code, the modulus of $\tilde{\phi}$ is very well aligned with the amplitude of the magnetic field and the Jacobian. With HSX, the effects of the helical symmetric of the configuration are also well shown. But the toroidal variation of $\tilde{\phi}$ does not seem to be correlated with the shape of B. However, it reaches its maximum (the central spot around $\varphi = \pi/4$ and $\theta^* = \pi$) where $\sqrt{g}^*$ is minimum. The structure of the ITG driven mode results from the combined effects of $\sqrt{g}^*$ which is strongly varying along the toroidal direction and the almost helical magnetic field. With $N = 35$, we can observe the transition between the quasi-helical and helical systems. Here the mode is still strongly helical, but its shape is also affected by the difference of structure between the Jacobian and the amplitude of the magnetic field.

HSX being characterized by a helical magnetic axis, the structure of the Jacobian results from the variation of the position of the magnetic axis along the toroidal direction. As shown in Fig. 7, the poloidal plane is centered around $R = 1.45$m at $\varphi = 0$ whereas it is centered around $R = 1.05m$ at $\varphi = \pi/N_{per}$. The curvature drifts

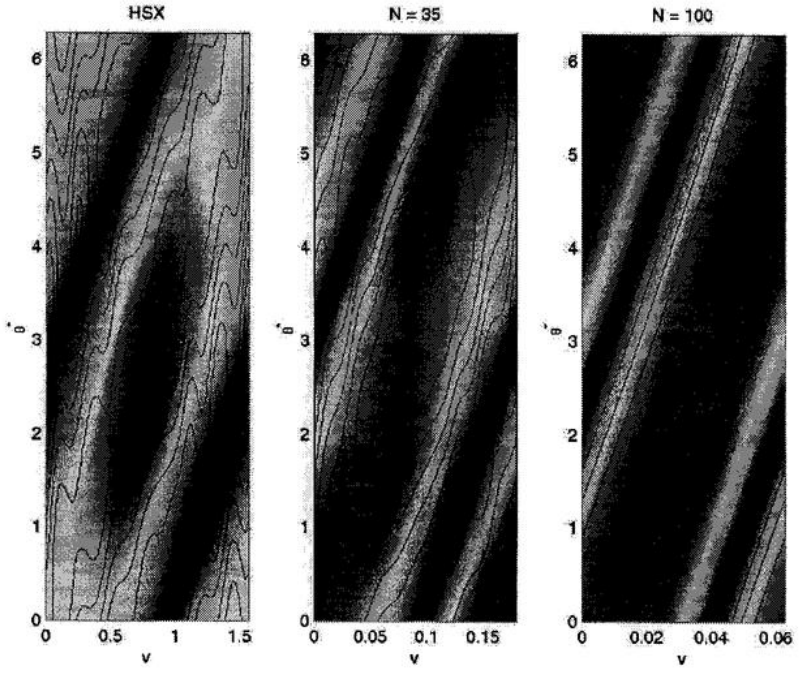

Figure 8: *Amplitude of the extracted potential* $\tilde{\phi}$ *and* B *(continuous lines) as a function of* φ *(denoted* v*) and* θ^* *measured at* $s = s_0$ *with* $N = 4$ *(HSX),* $N = 35$ *and* $N = 100$.

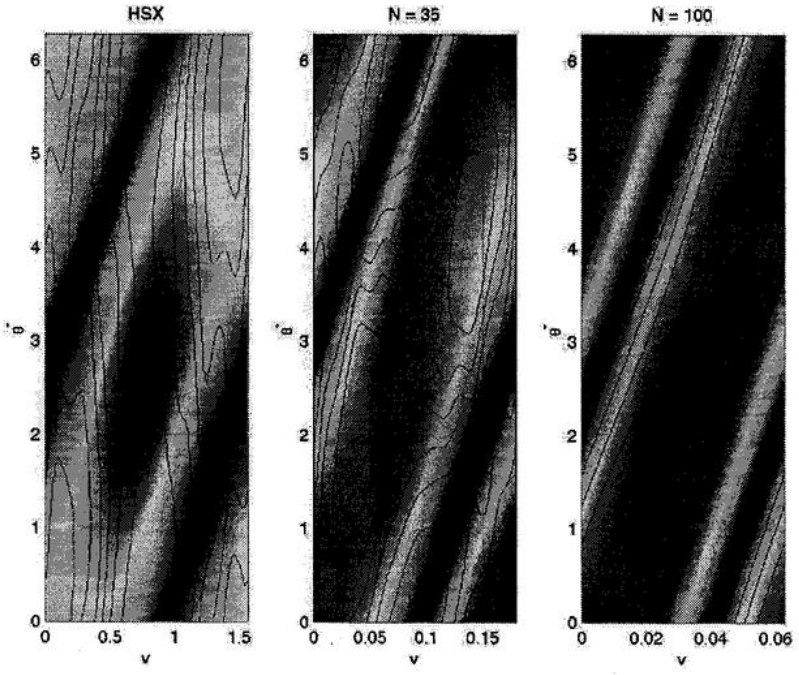

Figure 9: *Amplitude of the extracted potential* $\tilde{\phi}$ *and* $\sqrt{g}^*$ *(continuous lines) measured at* $s = s_0$ *with* $N = 4$ *(HSX),* $N = 35$ *and* $N = 100$.

are then stronger at the middle of the period. However, the effects of this feature of HSX on the frequency and growth rate of the ITG driven mode are not clearly established and require further simulations.

5 Conclusions

We have investigated the linear stability properties of the ITG driven modes in two different 3D configurations with the help of the 3D global gyrokinetic code EUTERPE. Our model based on gyrokinetic ions and adiabatic electrons has revealed an interesting feature of the electrostatic ITG instability. In the QAS3 configuration, results do not show a strong effect resulting from the 3D geometry on the growth rate, the frequency and the shape of the ITG driven mode. Here, the ITG driven mode is ballooning in the outer part of the torus where the amplitude of the magnetic field is almost constant along the toroidal direction. The results are then similar to those of a tokamak. On the other hand, HSX which is not dominated by toroidal effects has shown a clear and new 3D effect related to the 3D shape of the plasma, i.e. the variation of the centrifugal force along the magnetic field lines. However, here again, this effect on the growth rate of the ITG driven mode has turned out to be weak. Further simulations are required to validate this point.

However, the physical model needs to be improved by including a non adiabatic response of the electrons, because with our current model we miss all the important destabilizing effects due to trapped electrons. Furthermore, we should include the effects of an equilibrium radial electric field, as in tokamaks it has a strong stabilizing influence on the ITG driven mode.

Acknowledgment: This work was partly supported by the Swiss National Science Foundation. The computations have been performed on the CRAY T3E of the Joint Computing Center of the Max Planck Gesellschaft and the IPP in Garching and the Origin 2000 of the Ecole Polytechnique Fédérale de Lausanne.

References

[1] M. Kick *et al.*, Plasma Phys. Control. Fusion **41**, (1999) A549.

[2] A. Bhattacharjee *et al.*, Phys. Fluids **26**, (1983) 880.

[3] N. Dominguez, B.A. Carreras and V.E. Lynch, Phys. Fluids B **4**, (1992) 2894.

[4] R.E. Waltz and A.H. Boozer, Phys. Fluids B **5**, (1993) 2201.

[5] M. Persson, J.L.V. Lewandowski and H. Nordman, Phys. Plasmas **3**, (1996) 3720.

[6] J.L.V. Lewandowski, Phys. Plasmas **4**, (1997) 4023.

[7] A. Kendl and H. Wobig, Phys. Plasmas **6**, (1999) 4714.

[8] G. Rewoldt, L. P. Ku, W. M. Tang and W. A. Cooper, Phys. Plasmas **6**, (1999) 4705.

[9] J. Nührenberg and R. Zille, Phys. Lett. A., **129**, (1988) 113.

[10] G . Jost *et al.*, in *Theory of fusion plasmas, Int. Workshop, Varenna, September 1998* (Editrice Compositori, Società Italiana di Fisica, Bologna, 1999) p 419.

[11] G. Jost *et al.*, in *Proc. 26th EPS Conf. on Controlled Fusion and Plasma Physics, Maastricht, 1999* p 1093.

[12] S. P. Hirshman and D. K. Lee, Comp. Phys. Comm. **39**, (1986) 161.

[13] P. Garabedian and L. P. Ku, Phys. Plasmas **6**, 645 (1999).

[14] F. S. B. Anderson *et al.*, Trans. Fusion Tech., **27**, (1995) 273.

[15] R. C. Grimm, J. M. Greene, and J. L. Johnson, Methods in Comp. Phys. **16**, (1976) 253.

[16] T.S. Hahm, Phys. Fluids **31**, (1988) 2670.

[17] M. Fivaz *et al.*, Comp. Phys. Comm. **111**, (1998) 27.

[18] T.M. Tran *et al.*, in *Theory of fusion plasmas, Int. Workshop, Varenna, September 1998* (Editrice Compositori, Società Italiana di Fisica, Bologna, 1999) p 45.

[19] S. Brunner, Ph. D. Thesis **1701**, Ecole Polytechnique Fédérale de Lasaunne, (1997).

[20] J. Nührenberg, W. Lotz and S. Gori, in *Theory of fusion plasmas, Int. Workshop, Varenna, August 1994* (Editrice Compositori, Società Italiana di Fisica, Bologna, 1995) p 3.

[21] W. A. Cooper, Phys. Plasmas **7**, (2000) 2546.

[22] J. Nührenberg and R. Zille in *Theory of fusion plasmas, Int. Workshop, Varenna, August 1992* (Editrice Compositori, Società Italiana di Fisica, Bologna, 1993) p 17.

Linear gyrokinetic simulations using particles for small perpendicular wavelength perturbations

A. Bottino, T.M. Tran, O. Sauter, J. Vaclavik and L. Villard
Centre de Recherches en Physique des Plasmas, Association Euratom - Confédération Suisse, Ecole Polytechnique Fédérale de Lausanne PPB, CH-1015 Lausanne, Switzerland

Microinstabilities are widely considered a possible source of anomalous transport in tokamaks. High order finite Larmor radius (FLR) effects have been included in a linear 2D gyrokinetic Particle-In-Cell (PIC) code for the study of the time evolution of electrostatic, quasi-neutral perturbations in realistic tokamak geometries. This has been done using a Padé approximation of Bessel functions in the quasi-neutrality equation. This extends the validity range of our PIC code over previous versions which had FLR effects only up to second order in $k_\perp \rho$. Trapped electrons dynamics has been modelled using a drift-kinetic approximation. Axisymmetric equilibria are provided by the MHD equilibrium code CHEASE [1].

1. Introduction

During the past years, the CRPP theory group has developed several Particle In cell (PIC) codes in 2D and 3D configurations [2, 3, 4, 5] in order to study low frequency electrostatic microinstabilities in laboratory plasmas. The time evolution, particle in cell (PIC) approach for solving global gyrokinetic equations permits us to find very efficiently the most unstable mode for a given equilibrium. Moreover, the use of a finite element representation for the potential allows us to work with realistic equilibria. All these codes contain finite Larmor radius (FLR) effects only to second order. This limitation can be relaxed using a Padé approximation instead of a Taylor expansion in the quasi-neutrality equation; this allows us to make reliable predictions of growth rates and real frequencies for instabilities with $k_\perp \rho \geq 1$.

In this paper we present simulations of ion temperature gradient (ITG) and trapped electron mode (TEM) instabilities with perpendicular wavelengths of the same order as the ion Larmor radius for realistic tokamak configurations. The physical model implemented here is based on the gyrokinetic equation for the ions, the quasi-neutrality condition and electrostatic perturbations. A drift-kinetic model is used to describe trapped electrons dynamics while the passing electrons are assumed to respond adiabatically.

2. The model

We describe ion dynamics with a gyrokinetic model derived by Hahm [6] based on a Vlasov-Poisson system in which the fast ion cyclotron motion has been averaged out. This model is particularly suitable for particle simulations because it preserves the Hamiltonian structure of the original equations. In this regime the particle guiding centers are well defined and the time evolution of the perturbed distribution function $\tilde{f}$ depends on the unperturbed guiding center trajectories:

$$\frac{\partial \tilde{f}}{\partial t} + \dot{\vec{R}} \cdot \nabla \tilde{f} + \dot{v_{\|}} \frac{\partial \tilde{f}}{\partial v_{\|}} = F(\vec{E});$$

with

$$\begin{aligned} F(\vec{E}) = & - \frac{\langle \vec{E} \rangle \times \vec{h}}{B^*} \frac{\partial f_0}{\partial t} - \frac{q_i \langle \vec{E} \rangle}{m_i} \cdot \vec{h} \frac{\partial f_0}{\partial v_{\|}} - \\ & - \left(v_{\|} \frac{\partial f_0}{\partial v_{\|}} + \frac{1}{2} v_{\perp} \frac{\partial f_0}{\partial v_{\perp}} \right) \langle \vec{E} \rangle \cdot \frac{\vec{h} \times \nabla B}{B^*}; \\ \vec{h} = & \frac{\vec{B}}{B}. \end{aligned}$$

The unperturbed guiding center trajectories are given by:

$$\begin{aligned} \dot{\vec{R}} &= \vec{v}_{GC} = v_{\|} \vec{h} + \frac{1}{\Omega} (\mu B + v_{\|}^2) \frac{\vec{h} \times \nabla B}{B^*}; \\ \dot{v_{\|}} &= -\mu \vec{h} \cdot \nabla B; \end{aligned}$$

where

$$\begin{aligned} f &= \tilde{f} + f_0; \\ B^* &= B + \frac{m_i v_{\|}}{q_i} \vec{h} \cdot \nabla \times \vec{h}. \end{aligned}$$

The gyro-averaged electric field at the ion guiding center $\vec{R} = \vec{r} - \vec{\rho}$ is :

$$\langle \vec{E} \rangle (\vec{R}, \mu, t) = -\frac{1}{2\pi} \int \vec{\nabla} \phi(\vec{x}, t) \delta(\vec{R} + \vec{\rho} - \vec{x}) d\alpha d\vec{x};$$

Trapped electrons are modeled using drift-kinetic equations ($\rho_e = 0$) while passing electrons are assumed to respond adiabatically to the perturbation.

The quasi-neutrality constraint $\tilde{n}_e = \tilde{n}_i$ is used to close the system, with

$$\tilde{n}_e = n_0 (1 - \alpha_b) \frac{e\phi}{T_e} + \int_{trapped} d^6 z B^* \delta(\vec{R} + \vec{\rho} - \vec{x}) \tilde{f}_e;$$

$$d^6 z = d\alpha d\mu dv_{\|} d\vec{R};$$

the parameter α_b is the fraction of trapped particles at a given point in the plasma,

$$\alpha_b = \sqrt{1 - \frac{B(s,\theta)}{B_{max}(s)}}$$

and

$$\tilde{n}_i = \bar{n}_i + n_{pol};$$
$$\bar{n}_i = \int \tilde{f}(\vec{R}, v_{\|}, \mu)\delta(\vec{R} - \vec{x} + \vec{\rho})d^6z;$$

$$n_{pol}(\vec{x}) = q_i/m_i \int B^*\delta(\vec{R} - \vec{x} + \vec{\rho})(\phi - \langle\phi\rangle)d^6z.$$

Assuming $k_\perp\rho << 1$ we can expand the delta functions in the polarization density around $\vec{R} - \vec{x}$. The integral over all the velocity variables can now be performed and this gives:

$$n_{pol}(\vec{x}) = \nabla_\perp \cdot \left(\frac{n_0}{B\Omega}\nabla_\perp\phi(\vec{x})\right)$$

where n_0 represents the ion guiding center density. This expression is valid to the order of $(k_\perp\rho)^2$. The corresponding quasi-neutrality equation is :

$$\tilde{n}_i - \tilde{n}_e = \nabla_\perp \cdot \left(\frac{n_0}{B\Omega}\nabla_\perp\phi\right). \tag{1}$$

An alternative representation of n_{pol} has been given by taking a Fourier decomposition for the electrostatic potential and then integrating it over velocity space. For uniform n_0 and T_i profiles this leads to

$$n_{pol,\vec{k}} = -\frac{n_0 q_i}{T_i}\left[1 - e^{-k_\perp^2\rho^2} I_0(k_\perp^2\rho^2)\right]\phi_{\vec{k}}$$

Performing a Padé approximation of this function, we get

$$n_{pol,\vec{k}} = -\frac{n_0 q_i}{T_i}\frac{(k_\perp\rho)^2}{1 + (k_\perp\rho)^2}\phi_{\vec{k}}$$

Therefore, in the general case, the quasi-neutrality equation becomes

$$(1 - \nabla_\perp\frac{T_i}{m_i\Omega^2}\nabla_\perp)(\tilde{n}_i - \tilde{n}_e) = \nabla_\perp \cdot \left(\frac{n_0}{B\Omega}\nabla_\perp\phi\right) \tag{2}$$

In the numerical implementation, integrals over the gyroangle are approximated with a discrete sum. A four-point discrete sum has been shown [7] to be sufficient for perturbations with $k_\perp\rho < 2$, this is correct to the order $(k_\perp\rho)^2$ at which (1) is correct. Therefore, the number of averaging points is increased for consistency with the Padé approximation.

3. Results

In our model, the MHD equilibrium code CHEASE [1] provides the magnetic field and allows us to study microinstabilities in realistic plasmas. In these simulations we have used analytical temperature and density profiles given by:

$$\frac{1}{T}\frac{dT}{ds} = -K_T cosh^{-2}\left(\frac{s - s_0}{\Delta s_T}\right);$$
$$\frac{1}{n}\frac{dn}{ds} = -K_n cosh^{-2}\left(\frac{s - s_0}{\Delta s_n}\right);$$

with $s = \sqrt{\psi/\psi_{edge}}$, a radial coordinate, and ψ is the poloidal flux.
All the results shown in this section correspond to an equilibrium with global parameters $s_0 = 0.6$, $\Delta s_n = 0.35$, $\Delta s_T = 0.20$, $\eta_e = 2$, $K_{ni} = K_{ne} = 1.25$, $m_i/m_e = 40$, $B_0 = 1.0T$, $R_0 = 1.0m$ and $\epsilon = a/R_0 = 0.25$. The simulation provides the growth rate, real frequency and radial structure of the most unstable mode for a given toroidal mode number n.
In Fig.(1) we show a comparison between results obtained with the two different approximations of the quasi-neutrality equation with drift-kinetic trapped electrons for $\eta_i \equiv K_{Ti}/K_{ni} = 3.5$. A case with purely adiabatic electron response is also shown. For this value of η_i the most unstable mode is an ITG ; taking into account trapped electrons dynamics the resulting mode still propagates in the ion diamagnetic direction and corresponds essentially to a toroidal-ITG perturbed by trapped electrons (ITG+TEM).

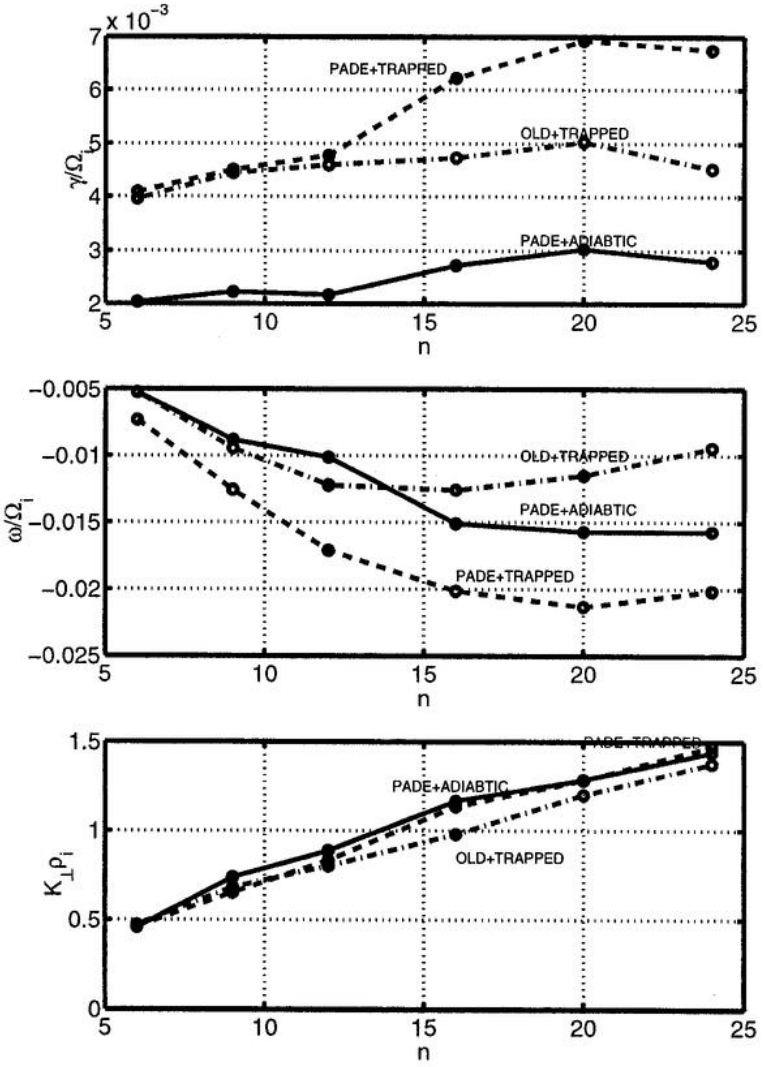

Figure 1: Comparison between the Padé and the $O(k_\perp\rho)^2$ approximation. Growth rates, real frequencies and averaged $k_\perp\rho_i$ for $\eta_i = 3.5$ for an ITG mode with drift-kinetic or adiabatic trapped electrons.

The effect of Padé approximation is evident for $n > 12$; this corresponds to $k_\perp\rho \geq 0.8$. The analysis of the structures in the poloidal plane shows that the radial position of the mode is

not affected by the choice of the approximation.
In Fig.(2) we present a scan on η_i for different n using the same equilibrium parameters as in Fig.(1). Decreasing η_i, the most unstable mode undergoes a transition to a predominantly TEM, the pure ITG mode being stabilized below a critical η_i value; the real part of the frequency changes sign implying that the mode propagates in the electron diamagnetic direction. The critical η_i value at which trapped electron dynamics effects start to dominate the time evolution of the instability increases with n.

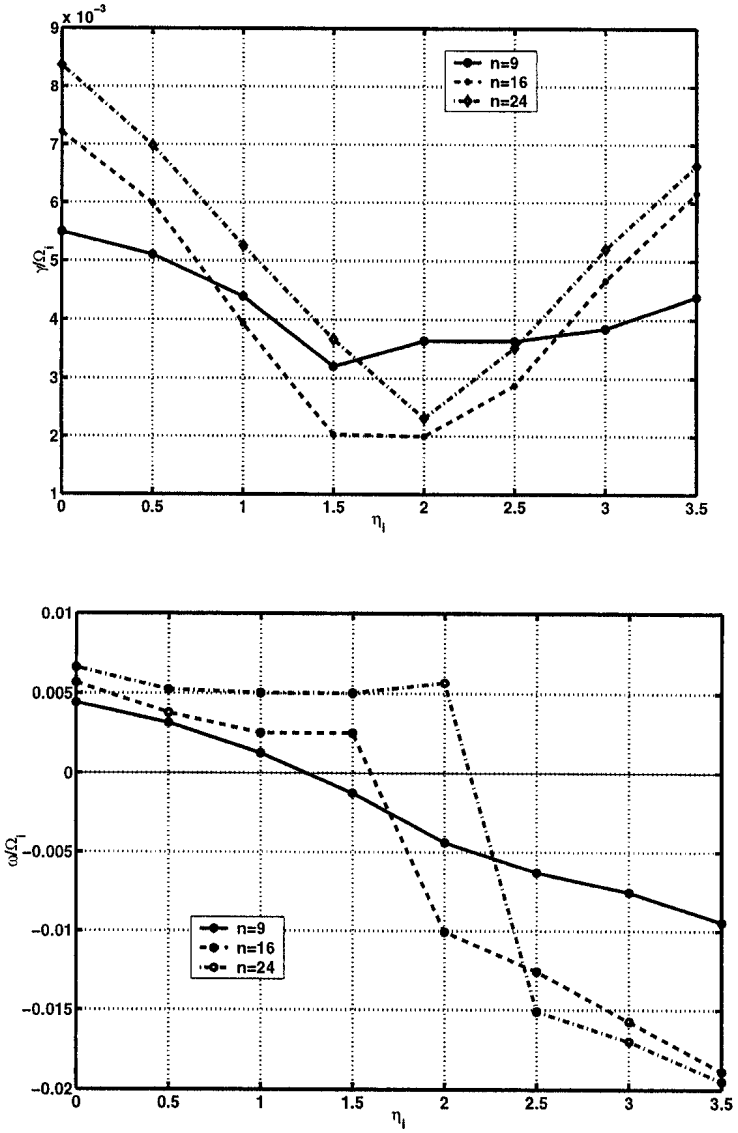

Figure 2: Growth rates and real frequencies for n=9, n=16, n=24, as a function of η_i, using Padé approximation.

Some mode structures, in the poloidal plane for $n = 9$ and $n = 24$, are shown in Fig.(3); a little change in the mode structure can be seen at the transition from TEM to ITG.

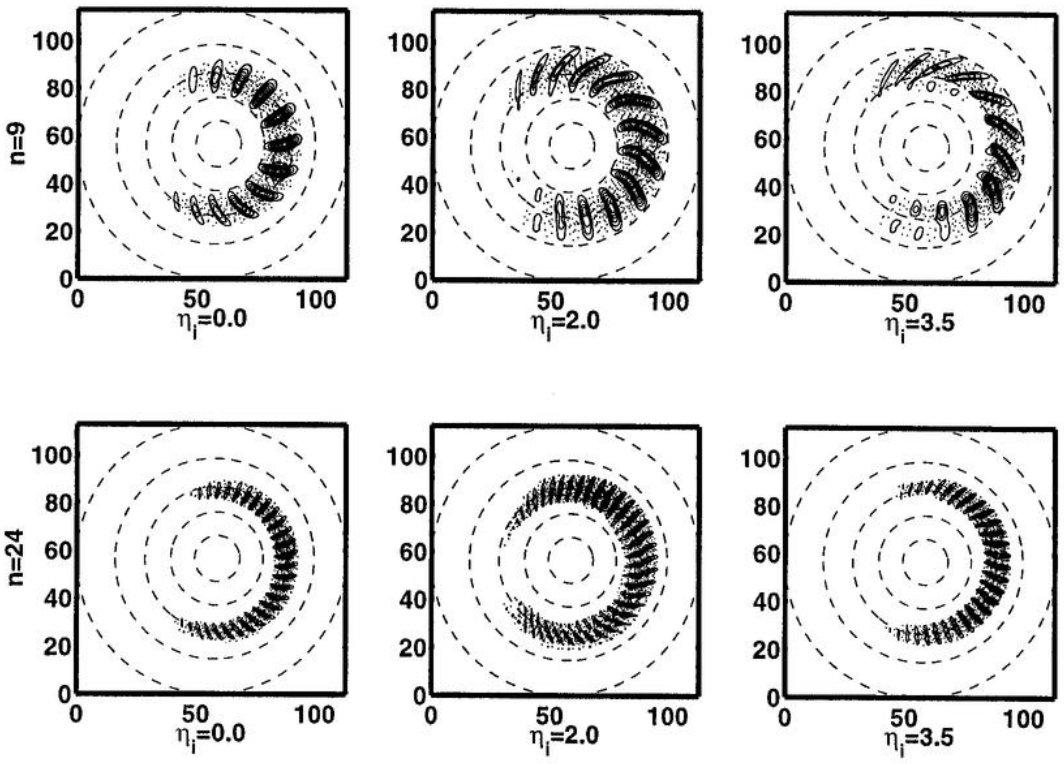

Figure 3: Mode structures in the poloidal plane for two different values of n. For $\eta_i = 2.0$, the mode corresponding to $n = 9$ shows a typical ITG behavior, while for $n = 24$ trapped electrons effects dominate the instability growth.

References

[1] H. Lütjens, A. Bondeson and O. Sauter, Comput. Phys. Commun. **97**, 219 (1996)

[2] M. Fivaz *et al.*, Comput. Phys. Commun. **111**, 27 (1998)

[3] T.M. Tran *et al.*, in *Theory of fusion plasmas. Int. Workshop, Varenna, August 1998*, p. 45 (Editrice Compositori, Societa' italiana di Fisica, Bologna, 1999)

[4] L. Villard *et al.*, in *Theory of fusion plasmas. Int. Workshop, Varenna, August 1998*, p. 427 (Editrice Compositori, Societa' italiana di Fisica, Bologna, 1999)

[5] G. Jost *et al.*, this workshop

[6] T.S. Hahm, Phys. Fluids **31**, 2670 (1998)

[7] W.W. Lee, Journal of Comp. Phys. **72**, 243 (1987)

EFFECTS OF FINITE β ON THE LINEAR STABILITY OF ION TEMPERATURE GRADIENT (ITG) MODES

G.L. Falchetto and J. Vaclavik

Centre de Recherches en Physique des Plasmas
Association Euratom - Confédération Suisse
Ecole Polytechnique Fédérale de Lausanne
Lausanne, Switzerland

1. Introduction.

Recent experimental studies have shown the importance of finite β effects for energy transport, therefore a study of the electromagnetic effects on microinstabilities has been performed.

The gyrokinetic equation has been generalized to the electromagnetic case, by including the parallel component of the vector potential. Electron dynamics has been taken into account with the drift-kinetic approximation, including also trapped electrons. The plasma is thus described by the quasi-neutrality equation and the parallel component of Ampere's law. The two-equations system is then resolved globally by means of a spectral approach.

Results from the electromagnetic extension of the existing global gyrokinetic spectral code, GLOGYSTO [1], are presented here: they show the stabilizing role of finite β on toroidal ion temperature gradient (ITG) modes, even in presence of trapped electrons; trapped electrons modes (TEM), which are essentially electrostatic drift waves propagating in the electron diamagnetic direction, are on the contrary unaffected.

A study for different magnetic shear profiles, including negative shear, is also presented; results are in agreement with the electrostatic case: even in the presence of finite β, negative magnetic shear does not account for a complete stabilization of the ITG modes.

2. Electromagnetic Gyrokinetic Formalism.

A low-frequency electromagnetic perturbation is applied to a low β, toroidal plasma. We consider the case of a large aspect ratio tokamak with circular concentric flux surfaces, modelling ions as gyrokinetic and taking into account non-adiabatic electron dynamics.

The plasma can be described by the quasi-neutrality equation and the parallel component of Ampère's law:

$$\nabla^2{}_\perp A_\parallel = \mu_0 \sum_j q_j \int d\vec{v}\, v_\parallel\, g_j, \tag{1}$$

g_j is the non-adiabatic part of the perturbed distribution function for each species j of particles, which can be derived as the solution of the linearized electromagnetic gyrokinetic equation .This equation in gyro-center variables reads:

$$g_j\left(\vec{R},\vec{v};\omega\right) = \frac{q_j}{T_j} F_{Mj} \int d\vec{k}\, e^{i\vec{k}\cdot\vec{R}}\, J_0\Big(\frac{k_\perp v_\perp}{\Omega_{cj}}\Big)\,(\omega-\omega^{*j})\, i\mathcal{P}\,\left(\hat{\phi}(\vec{k}) - v_\parallel \hat{A}_\parallel(\vec{k})\right). \tag{2}$$

The propagator $\mathcal{P}$ is the same as in the electrostatic case (see eq.7 in [1]).

The Laplacian, LHF of eq.(1), has been approximated retaining first order terms in inverse aspect ratio, in particular it is evaluated by first Fourier developing the vector potential, using a decomposition adapted to the toroidal geometry, and then applying the operator :

$$\nabla^2{}_\perp A_\parallel = \sum_{(k,m)} -\left(\kappa^2 + \frac{m^2}{\rho^2}\right) \hat{A}_{\parallel(k,m)} \exp\{i\,(\kappa\rho + m\theta + n\varphi)\} \tag{3}$$

To evaluate the perturbed particle density and the RHS of parallel Ampère's law, we have to derive an explicit propagator expression for each species of particles and integrate over velocity space, after transforming back to particle variables.

2.1 Ions. For highly passing ions the explicit expression of the propagator is the same as the electrostatic one, the only difference is that it will be integrated over velocities being multiplied either by $v_\parallel$ or $v_\parallel^2$.

2.2 Electrons. Electrons are divided into two populations, highly passing and trapped; the propagator solution is thus derived in different ways for each of them: trapped electron dynamics is modeled as in the original electrostatic case, by means of a bounce-averaged drift-kinetic equation (eqs.42-45 in [1]) while for highly passing electrons we make use of a drift-kinetic approximation.

Considering that electron transit frequency is much higher than the mode frequencies

we are studying, we are allowed to approximate the propagator expression by retaining just lower electron transit frequency harmonics, i.e. $p = 0, \pm 1$. The poloidal coupling effect is then retained but it will concern only contiguous poloidal wave numbers : $m' = m, m \pm 1$. Moreover we take the local approximation $k_{\|} \simeq 1/R\,q_s$. The following expressions are obtained for the non-adiabatic contribution of circulating electrons respectively to the density fluctuation and to the parallel current (RHS of eq.1):

$$\tilde{n}_{Pe}^{n.a.} = -\frac{e}{T_e} \int d\vec{k}\, e^{i\vec{k}\cdot\vec{r}} \left(\omega - \omega_{ne}\right) R\,q_s\, \delta_m^{m'}\, A_{\|}(\vec{k}), \tag{4}$$

$$\begin{aligned} q_e \int d\vec{v}\, v_{\|}\, g_e = &-\frac{e^2}{T_e} \int d\vec{k}\, e^{i\vec{k}\cdot\vec{r}} \left(\omega - \omega_{ne}\right) R\,q_s\, \delta_m^{m'}\, \Phi(\vec{k}) \\ &+ \frac{e^2}{T_e} \int d\vec{k}\, e^{i\vec{k}\cdot\vec{r}} \Big[\omega \left(\omega - \omega_{ne}\right) (R\,q_s)^2\, \delta_m^{m'} \qquad (5) \\ &- \frac{k_\perp\, \rho_{Le}}{2}\, v_{the}\, R\,{q_s}^2 \left(\omega - \omega_{ne}\,(1 + \eta_e)\right)\left(\delta_m^{m'+1} + \delta_m^{m'-1}\right)\Big]\, A_{\|}(\vec{k}). \end{aligned}$$

3. Numerical Results.

A hydrogen plasma with dimensions similar to DIII-D is chosen, having thus the following magnetic geometry: $B_0 = 1.\,\text{Tesla}, R = 2.\,m, a = 0.5\,m$, with a safety factor profile $q_s(s) = 1.25 + 0.67s^2 + 2.38s^3 - 0.06s^4$, which besides verifies $q_s(s_0) = 2$, $\hat{s}(s_0) = 1$, $s_0 = 0.6$, s being the normalized radial variable. The density profile and the identical electron and ion temperature variations are determined by:

$$\frac{N(s)}{N_0} = \exp\left(-\frac{a\Delta s_n}{L_{n0}} \tanh\frac{s - s_0}{\Delta s_n}\right) \qquad \frac{T(s)}{T_0} = \exp\left(-\frac{a\Delta s_T}{L_{T0}} \tanh\frac{s - s_0}{\Delta s_T}\right)$$

with $\Delta s_n = 0.35$, $L_{n0} = 0.4\,m, \Delta s_T = 0.20$, $L_{T0} = 0.2\,m$, $T_0 = 7.5\,KeV$.

Fixing $n = 7$, corresponding to the most unstable ITG electrostatic mode (for this set of parameters), a scan over β up to 6% has been carried out both for the case of only circulating particles and including also trapped electrons. In this last case a plasma containing 70% of trapped electrons has been considered.

We have thus been able to study the effect of finite β on ITG modes, modified or not by the trapped electron dynamics and on trapped electrons modes (TEM).

Results are in good agreement with local ones from a kinetic electromagnetic dispersion relation and show a strong stabilization of ITG modes even in the presence of trapped electrons. We can compare in fig.1 the ITG mode without trapped electrons (full line with $\star$), which stabilizes at $\beta = 4\%$, to the same mode with trapped electrons (full line with $\bullet$):even though the electrostatic mode growth rate is a factor ~ 5

larger, it is stabilized at the slightly higher value $\beta = 5.5\%$.

A scan over magnetic shear has also been carried out: holding the safety factor at $q_s(s_0) = 2$, different magnetic shear profiles have been obtained such that $\hat{s}(s_0) = \pm 1, \pm 0.5, 0$. Results for ITG modes with trapped electrons, are also plotted in fig.1. It is evident that for values of β up to 2%, negative shear is stabilizing, as in the electrostatic case, but the combined effect of negative magnetic shear and finite β can not account for a complete stabilization of ITG modes: negative shear modes are even less affected by electromagnetic effects than positive shear ones.

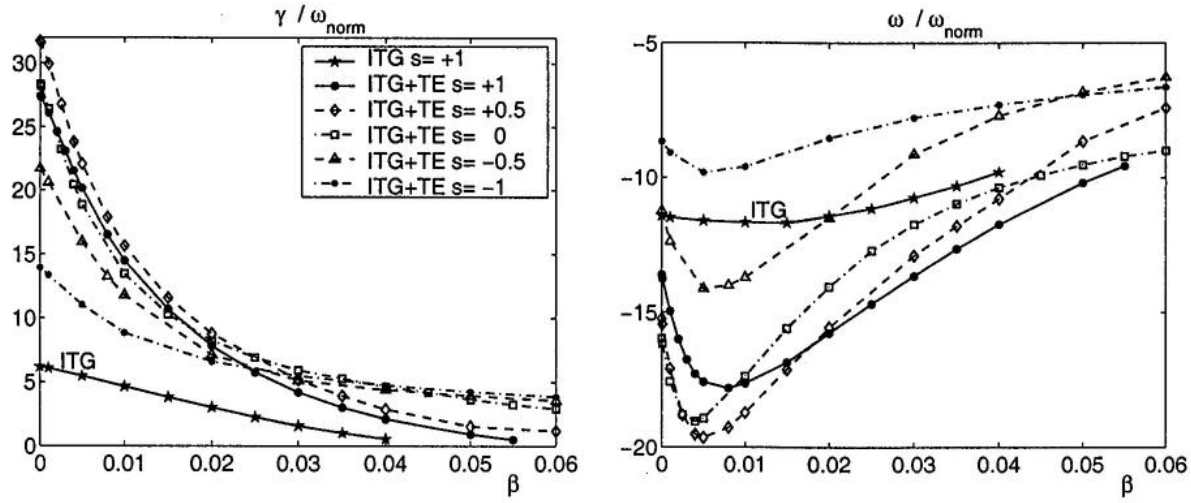

Figure 1: Normalized growth rates (left) and real frequencies (right) of an ITG mode with shear $\hat{s}(s_0) = 1$ (full line with $\star$) and ITG modes with trapped electrons (TE), for different shear profiles such as $\hat{s}(s_0) = \pm 1, \pm 0.5, 0$. ($\omega_{norm} = \rho_{Li}\, v_{thi}/a^2 \simeq 3 \cdot 10^4 Hz$)

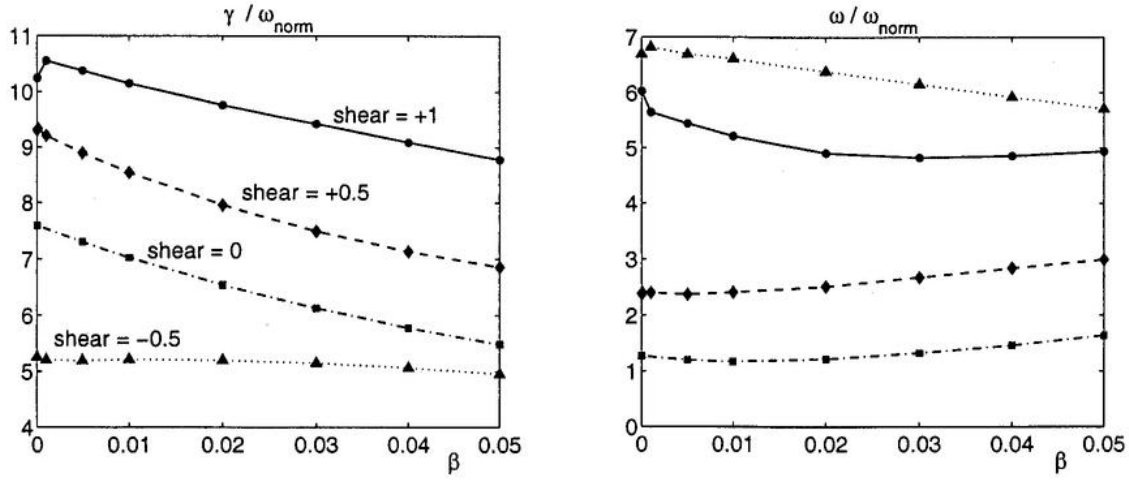

Figure 2: Normalized growth rates (left) and real frequencies (right) of TEM, for different shear profiles such as $\hat{s}(s_0) = 1, 0.5, 0, -0.5$. The mode is stable for $\hat{s}(s_0) < -0.5$.

larger, it is stabilized at the slightly higher value $\beta = 5.5\%$.

A scan over magnetic shear has also been carried out: holding the safety factor at $q_s(s_0) = 2$, different magnetic shear profiles have been obtained such that $\hat{s}(s_0) = \pm 1, \pm 0.5, 0$. Results for ITG modes with trapped electrons, are also plotted in fig.1. It is evident that for values of β up to 2%, negative shear is stabilizing, as in the electrostatic case, but the combined effect of negative magnetic shear and finite β can not account for a complete stabilization of ITG modes: negative shear modes are even less affected by electromagnetic effects than positive shear ones.

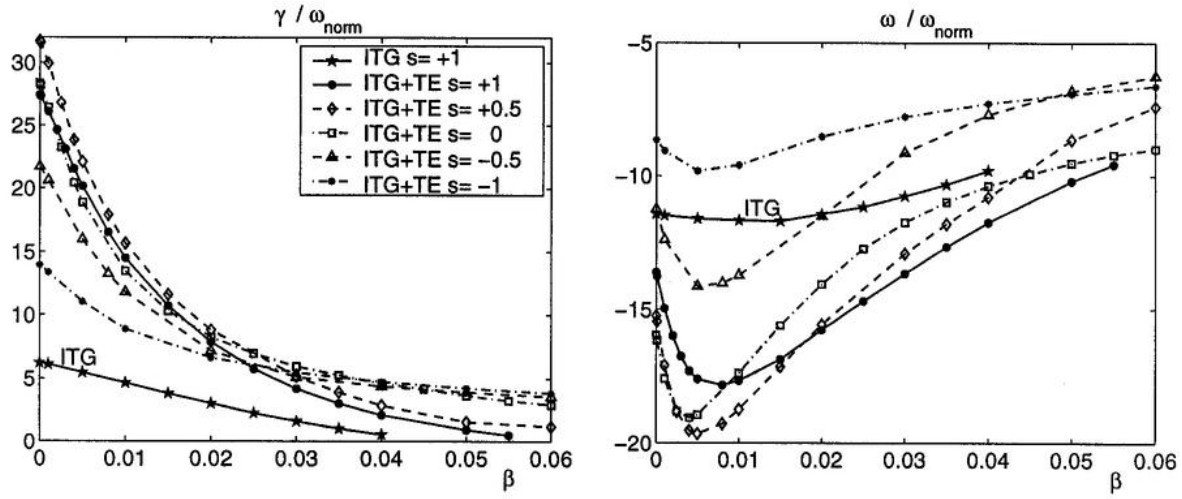

Figure 1: Normalized growth rates (left) and real frequencies (right) of an ITG mode with shear $\hat{s}(s_0) = 1$ (full line with $\star$) and ITG modes with trapped electrons (TE), for different shear profiles such as $\hat{s}(s_0) = \pm 1, \pm 0.5, 0$. ($\omega_{norm} = \rho_{Li}\, v_{thi}/a^2 \simeq 3 \cdot 10^4 Hz$)

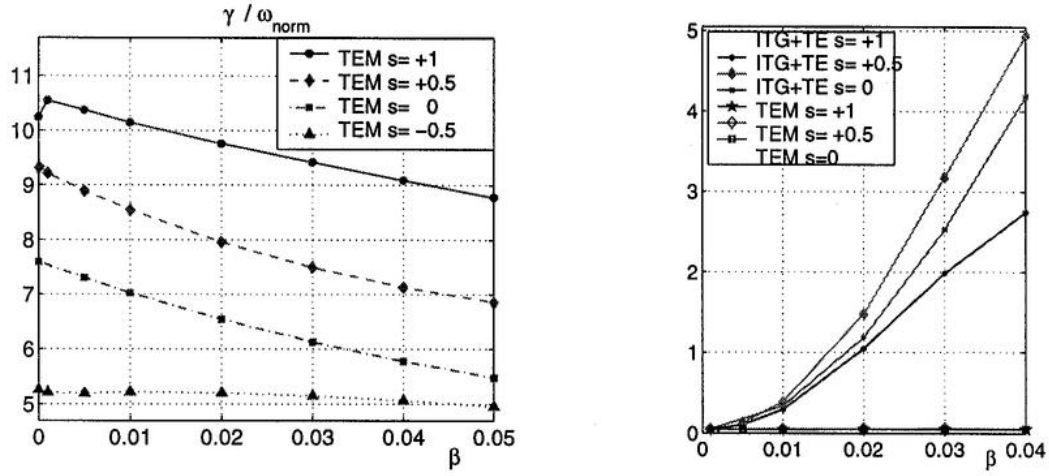

Figure 2: Normalized growth rates (left) and real frequencies (right) of TEM, for different shear profiles such as $\hat{s}(s_0) = 1, 0.5, 0, -0.5$. The mode is stable for $\hat{s}(s_0) < -0.5$.

Contrary to the ITG type instability, for which either there is a single mode or the most unstable mode is well isolated, the spectrum contains a set of very densely packed trapped electron modes propagating in the electron diamagnetic direction, we therefore followed just the most unstable TEM for each β value.

Fig.2 highlights the effect of β on TEM for different magnetic shear profiles: it is evident that TEM are slightly affected by electromagnetic effects; this could be explained by the essentially electrostatic character of these instabilities.

As regards negative magnetic shear, TEM are progressively damped, so that they are stable for values $\hat{s}(s_0) < -0.5$, similarly to the electrostatic case.

Finally in fig.3 we plot the structure in the poloidal plane of the electrostatic and vector potentials, of the most unstable ITG mode with trapped electrons, i.e. for $\hat{s}(s_0) = 0.5$ (dashed line with $\diamond$ of fig.1). It can be seen that as β increases the electrostatic potential looses more and more its ballooning structure and its localization at the rational surface $s_0 = 0.6$; the vector potential indeed does not change so much but its structure tends to be less centered around $\theta = 0$.

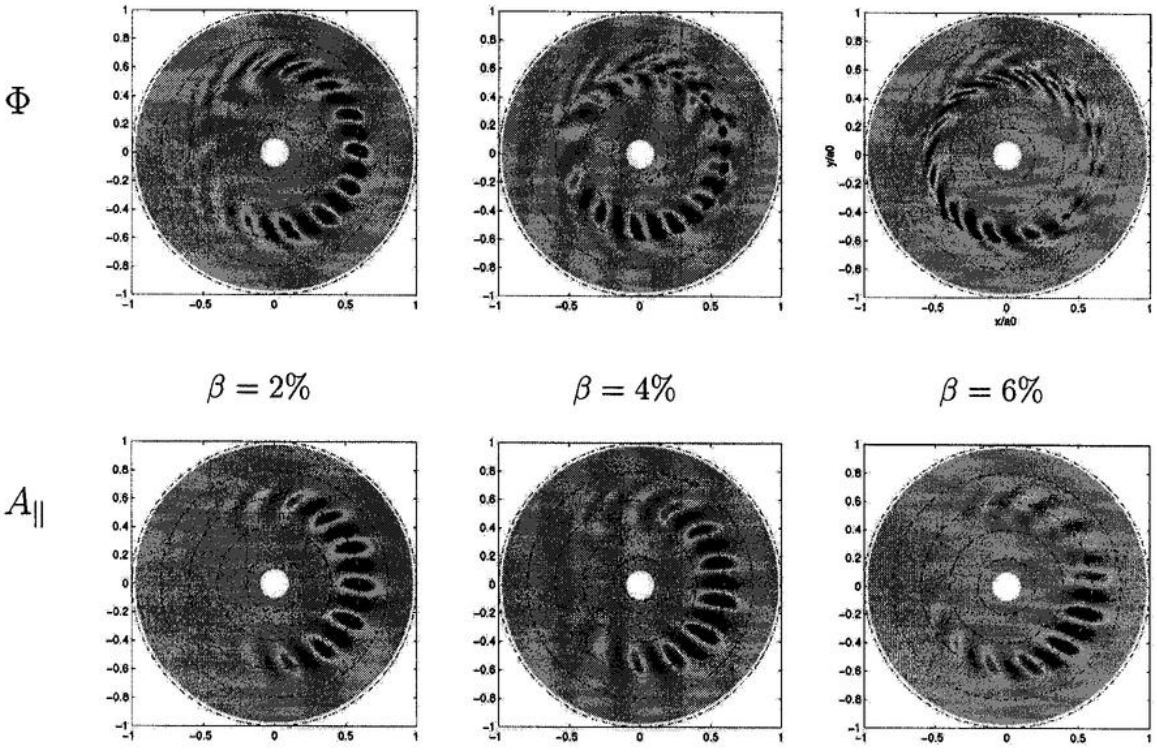

Figure 3: Poloidal contours of the electrostatic potential (top line) and vector potential (bottom line) of the most unstable ITG mode with trapped electrons, $\hat{s}(s_0) = 0.5$, for increasing values of β

4. Conclusion.

We have developed an electromagnetic version of the 2D global gyrokinetic spectral code GLOGYSTO, in order to study the effect of finite β on the global stability of ITG modes.

Results are in agreement with previous studies: electromagnetic effects are strongly stabilizing ITG modes even taking into account trapped electron dynamics, which has indeed a strong destabilising effect on the electrostatic ITG modes. The study has been also extended to TEM, over which finite β effects have just a little influence, which is not astonishing given the electrostatic character of these instabilities. Finally different magnetic shear profiles have been analyzed to study the combined effect of β and magnetic shear, eventually negative. Results are in good agreement with electrostatic cases: negative magnetic shear cannot account for a complete stabilization of ITG modes in presence of trapped electrons, while it does damp TEM; for values of β up to 2% it has nonetheless a stabilizing effect, while for higher values negative shear modes are less stabilized than positive shear ones.

We should point out that in this model electrons are treated with a drift-kinetic approximation; to properly study electromagnetic modes, such as kinetic ballooning modes for which the electron drive is as important as the ion one, gyrokinetic electrons will be needed; therefore this will represent a first further extension to this study, combined eventually with the introduction of Shafranov shift and $E \times B$ flow.

Acknowledgments. This work was supported in part by the Swiss National Science Foundation. The computations have been performed on the Origin2000 of the Ecole Polytechnique Fédérale de Lausanne

References

[1] S. Brunner, M. Fivaz, T.M. Tran and J. Vaclavik, Physics of Plasmas **5**(11), 3929, (1998)

CONFINEMENT STUDY OF A COMPACT QUASIAXISYMMETRIC TOROIDAL SYSTEM

O. Fischer, W.A. Cooper, M. Yu. Isaev*, L. Villard

Centre de Recherches en Physique des Plasmas, Association Euratom - Confédération Suisse, Ecole Polytechnique Fédérale de Lausanne, Lausanne, Switzerland

**Nuclear Fusion Institute, Russian Research Centre "Kurchatov Institute", 123182 Moscow, Russia*

1. Introduction. We have analyzed the behavior of the diffusion coefficient in a compact toroidal system for a sequence from an axisymmetric to a quasiaxisymmetric configuration (Tab. 1) and for different particle energies by using the **VENUS** code which has been benchmarked with the MCT code [1] and the GC3 code [2]. The equilibria have been computed with the fixed boundary VMEC code by imposing the ι-profile ($\iota(s) = 1 - 2/3 \cdot s$) and a β value of ~ 5.90 %. The geometry of the coils (Fig. 1) consists of 10 toroidal coils (TC) wound on a spherical structure of 1.1 $[m]$ radius. Inside the TC, 10 modular helical Furth-Hartman type coils are wound on a sphere of 1 $[m]$. Moreover, there are 2 vertical field coils (VF) in the polar region which compensate the current flowing in the toroidal arc segments. Two other VF are localized in the mid-plane to provide the plasma position. Moreover, we have studied the feasibility of a Sphellamak reactor design by analyzing the collisionless α-confinement and the diffusion coefficient for Deuterium ions. To realize it, we have multiplied the Fourier components R and Z that describe the last closed magnetic flux surface of the equilibria determined with the fixed boundary VMEC code by a factor of ten as well as the magnetic field strength.

2. Guiding centre drift orbits and the Monte Carlo evaluation of the diffusion coefficient. Boozer coordinates [3] have been used to evaluate the guiding centre drift orbits. In these coordinates, the magnetic field in the contravariant form is described by $\mathbf{B} = \boldsymbol{\nabla}\psi(s) \times \boldsymbol{\nabla}\vartheta + \boldsymbol{\nabla}\zeta \times \boldsymbol{\nabla}\chi(s)$

CONFIGURATION	$B_{00}\,[T]$	$I_{hc}\,[kA]$	$\beta\,\%$	$R\,[m]$	$a\,[m]$
Sphellamak 1	0.497	20	5.90	0.666	0.308
Sphellamak 2	0.467	60	5.88	0.699	0.322
Sphellamak 3	0.466	120	5.91	0.701	0.326
Sphellamak 4	0.473	180	5.88	0.702	0.321

Table 1: Characteristics of the configurations studied in the paper. I_{hc} corresponds to the current in the helical Furth-Hartman type coils.

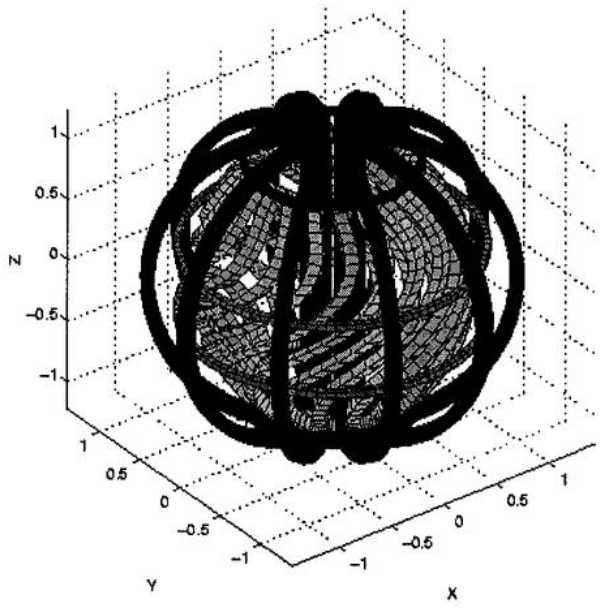

Figure 1: Coil system for the Sphellamak (ten toroidal coils, four verticals field coils and ten helical Furth-Hartman type coils).

where $s = \psi(s)/\psi_{edge}$, (ϑ, ζ) are the poloidal, toroidal coordinates and ψ (resp. χ) is the toroidal (resp. poloidal) flux function. In the covariant form, $\mathbf{B}$ is given by $\mathbf{B} = \mu_0 J(s)\boldsymbol{\nabla}\vartheta - \mu_0 I(s)\boldsymbol{\nabla}\zeta - \mu_0\nu(s,\vartheta,\zeta)\boldsymbol{\nabla}s$, with J (resp. I) the poloidal (resp. toroidal) current flux function and $\nu(s,\vartheta,\zeta)$ is a perdiodic function of ϑ and ζ.

By introducing e and m_0 the electronic charge and the rest mass of the particle, E_p the particle energy, μ the magnetic moment and $\rho_{\|} = p_{\|}/(eB)$, the equations of the guiding centre motion are given by [3, 4, 5]

$$\dot{s} = \frac{\mu_0 I(s)}{D_b}\Big[\big(\frac{\mu}{e} + \frac{eB}{m_0}\rho_{\|}^2\big)\frac{\partial B}{\partial \vartheta}\Big] + \frac{\mu_0 J(s)}{D_b}\Big[\big(\frac{\mu}{e} + \frac{eB}{m_0}\rho_{\|}^2\big)\frac{\partial B}{\partial \zeta}\Big], \tag{1a}$$

$$\dot{\vartheta} = \frac{eB^2\rho_{\|}}{m_0 D_b}\Big[\chi'(s) + \rho_{\|}\mu_0 I'(s)\Big] - \frac{\mu_0 I(s)}{D_b}\big(\frac{\mu}{e} + \frac{eB}{m_0}\rho_{\|}^2\big)\frac{\partial B}{\partial s}, \tag{1b}$$

$$\dot{\zeta} = \frac{eB^2\rho_{\|}}{m_0 D_b}\Big[\psi'(s) + \rho_{\|}\mu_0 J'(s)\Big] - \frac{\mu_0 J(s)}{D_b}\Big(\frac{\mu}{e} + \frac{eB}{m_0}\rho_{\|}^2\Big)\frac{\partial B}{\partial s}, \tag{1c}$$

$$\rho_{\|} = \pm\frac{1}{eB}\sqrt{2m_0(E_p - \mu B)}, \tag{1d}$$

where

$$D_b = \mu_0\Big[\chi'(s)J(s) - \psi'(s)I(s)\Big]\Big[1 + \mu_0\rho_{\|}\frac{J(s)I'(s) - I(s)J'(s)}{\chi'(s)J(s) - \psi'(s)I(s)}\Big].$$

The estimation of the diffusion coefficient is done by using Eq. (1a)-(1d) and applying a Lorentz scattering operator for the pitch angle at each time step of the integration [6]. We change the pitch angle $\lambda = v_{\|}/v$ from λ_0 to λ_n after a time step of length τ with the formula $\lambda_n = \lambda_0(1 - \nu\tau) \pm \sqrt{(1 - \lambda_0^2)\nu\tau}$ where ν is the deflection collision frequency defined in [6]. The symbol $\pm$ means the sign is to be chosen randomly. If the process is diffusive, the calculation of the dispersion $\sigma(t) =< (\Delta s(t))^2 > - < \Delta s(t) >^2$ with $\Delta s(t) = s(t) - s_0$ allows to estimate the diffusion coefficient $D = \sigma(t)/2t \cdot a^2$ as is mentioned in [7].

3. Numerical Results. The VENUS code has been benchmarked with the MCT code [1] by estimating the collisionless α-particles lost in W7X. For the simulation, we have used 2000 particles launched at $s_0 = 0.25$ with the poloidal, the toroidal and the pitch angles chosen randomly. Comparing Fig. 2a) with calculations done in [1], the VENUS code gives similar results. To check the Monte Carlo procedure to obtain the diffusion coefficient, we have estimated D for the TEXTOR Tokamak with Deuterium ions with $E_p = 500\,[eV]$ by assuming that the bulk of ions have the same temperature as the particle energy ($E_p = T$) and compare the VENUS results with the GC3 code [2, 8] and with the standard formula given in [9]. In Fig. 2b), we have plotted the analytic estimation of D by the solid line, the squares are the VENUS results and the circles are the GC3 estimation versus frequency. The VENUS results are very close to the analytic prediction.

The study of the Sphellamak has been realized by the estimation of D for the four configurations and for different particle (Deuterium) energies ($E_p = 30,\, 60\,[eV]$). For the simulations, we have used 10000 Deuterium particles launched at $s_0 = 0.25$ and the angles have been chosen randomly. As we can observe in Fig. 3a), D increases with respect to the helical deformation of the magnetic field strength (the I_{hc} value). This behavior has been observed in [8] for the MHH2. In Fig. 3b), we have made the same computations but with $E_p = 60\,[eV]$ and we remark that D has slightly increased compared to Fig. 3a). By estimating the collisionality regime ($\nu_{i*} = 4.90 \cdot$

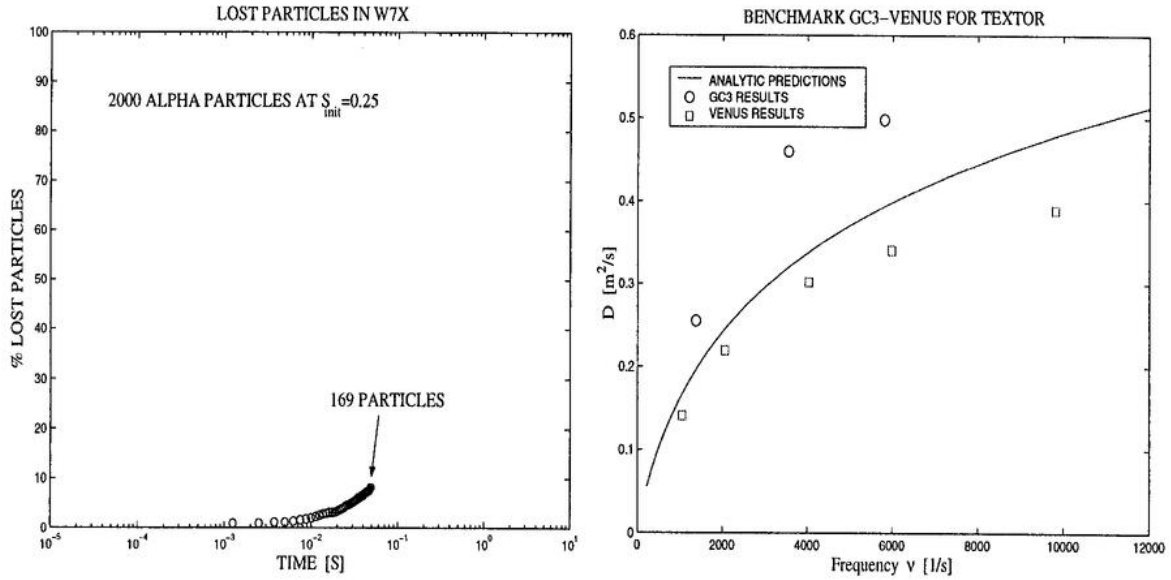

Figure 2: a) Percentage of lost α-collisionless particles in W7X estimated by the VENUS code versus time (left). b) Diffusion coefficient for the TEXTOR Tokamak estimated by the VENUS code (squares), by GC3 code (circles) and the theoretical formula (solid line) versus frequency (right).

$10^{-18} qRnZ^4 T^{-2} \epsilon^{-3/2} \log \Lambda$), we find that for these densities and energies, we are situated between the plateau and the Pfirsch-Schlüter regime which explains the close values of D for the four configurations.

Finally, we have studied the collisionless α-confinement and the diffusion coefficient of Deuterium ions ($E_p = T = 10\,[keV]$) in a Sphellamak reactor design. In Fig. 4a), we have plotted the lost particles (5000 particles launched at $s_0 = 0.25$) percentage versus time and we see that the Sphellamak 1 confined perfectly all the particles contrary to the Sphellamak 4 for which 10 % (most of them are trapped particles) are lost due to the magnetic field line ripple effects. The Fig. 4b) shows the behavior of the diffusion coefficient D versus the density. As we can observe, D increases with respect to the density for the Sphellamak 1 contrary to the Sphellamak 4 for which D decreases. The reason is that for these parameters (density, temperature, etc.), we are in the banana regime and the theory of neo-classical transport in Stellarators [8, 10] predict that $D \sim 1/n$ which is plotted by the solid line.

4. Conclusions. The VENUS code allows to analyze the confinement of particle as well as the estimation of the diffusion coefficient in 3D configurations. In this paper, we have presented the main characteristics of a sequence of Sphellamak from an axisymmetric to a quasiaxisymmetric case. We have obtained that the diffusion

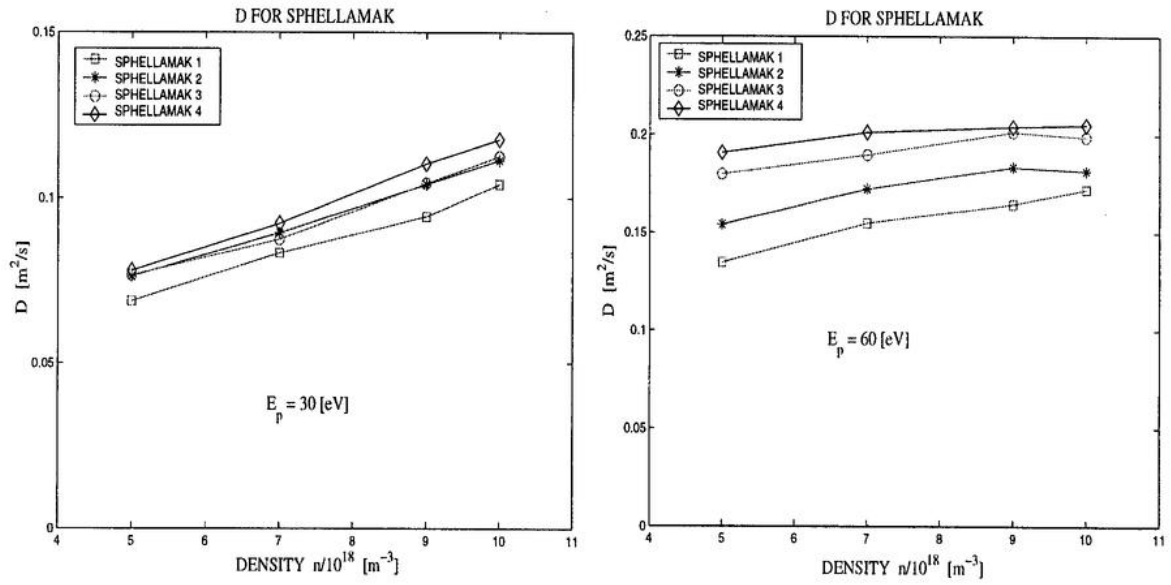

Figure 3: a) Diffusion coefficient for the Sphellamak for Deuterium particles energies with $E = 30\,[eV]$ (left) and b) $E = 60\,[eV]$ (right). (Squares: Sphellamak 1. Stars: Sphellamak 2. Circles: Sphellamak 3. Diamonds: Sphellamak 4).

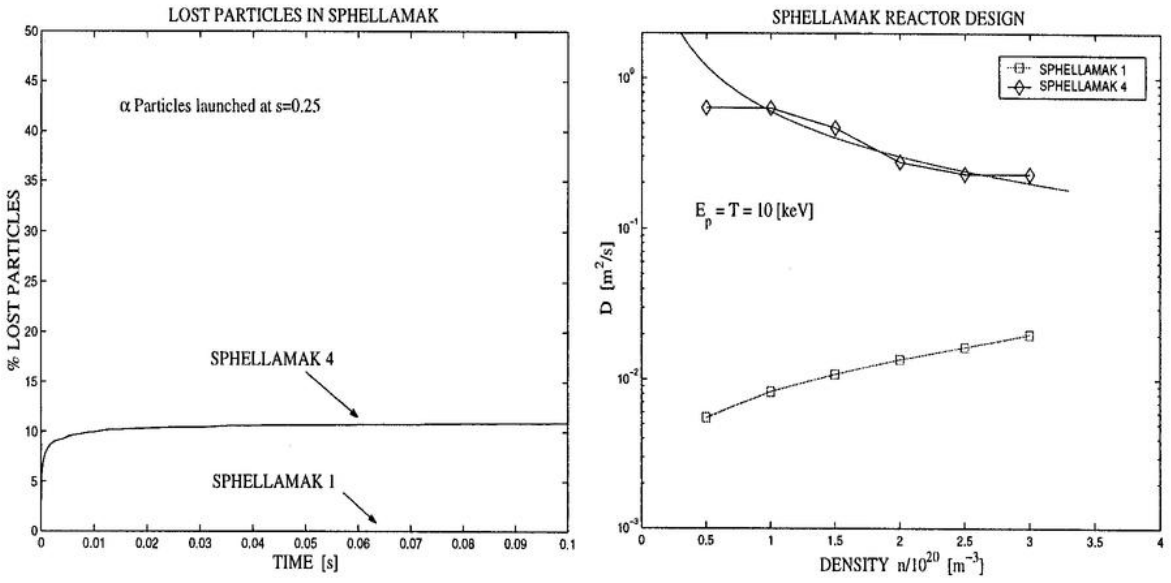

Figure 4: a) Percentage of lost α-collisionless particles in the Sphellamak 1 and in the Sphellamak 4 reactor design versus time (left). b) Diffusion coefficient for Deuterium ions with $E_p = T = 10\,[keV]$ in the Sphellamak 1 (squares) and in the Sphellamak 4 (diamonds) reactor design versus density (right). The solid line shows the behavior of $D \sim 1/n$.

coefficient D depends on the value of I_{hc} and on the particle energies. An increasing of I_{hc} leads a higher value for D due to the helical deformation of the magnetic field strength, but the diffusion coefficient for the Sphellamak 4 is still close to the axisymmetric configuration (Sphellamak 1) in the plateau, Pfirsch-Schlüter regime. Finally, we have shown the feasibility of a Sphellamak reactor design by analyzing D and the α-confinement. The estimation of D has proved that in the Sphellamak 1, D will increase with respect to the density. In the contrary, the Sphellamak 4 shows that the D will decrease due to the behavior of the banana particles in a helical magnetic field. Concerning the collisionless α-confinement in a Sphellamak reactor design, we have observed that the Sphellamak has good confinement properties and only the trapped particles are lost due to the magnetic field ripple, but it is a small fraction of the total particles.

We thank Dr. S. P. Hirshman for providing us with the VMEC code and Dr. H.Mynick for providing us with the GC3 code. The computations have been performed on the Origin2000 of the EPFL. This work was partially sponsored by the Fonds National Suisse de la Recherche Scientifique and by Euratom.

References

[1] Gori S., Lotz W., Nührenberg J., Theory of Fusion Plasmas, Varenna (1996) 335.

[2] Mynick H. E., Phys. Fluids **25** (1982) 325.

[3] Boozer A. H., Phys. Fluids **23** (1980) 904.

[4] Cooper W. A., Plasma Phys. Control. Fusion **39** (1997) 931.

[5] White R. B., Chance M. S., Phys. Fluids **27** (1984) 2455.

[6] Boozer A. H., Kuo-Petravic G., Phys. Fluids **24** (1981) 851.

[7] Fowler R. H., Rome J. A. and Lyon J. F., Phys. Fluids **28** (1985) 338.

[8] Mynick H. E., Plasma Phys. Reports **23** (1997) 547.

[9] Hinton F. L., Hazeltine R. D., Reviews of Modern Phys. **48** (1976) 239.

[10] Miyamoto K., Plasma Physics for Nuclear Fusion, MIT Press 1989.

Impurity transport in flux-driven models of edge turbulence

V. Grandgirard[1], O. Agullo[2], S. Benkadda[2], B. Biehler[3], X. Garbet[3], P. Ghendrih[3], Y. Sarazin[3]

[1] *Association Suisse-Euratom, CRPP-EPFL, PPB CH-1015 Ecublens, Switzerland.*

[2] *Equipe de Dynamique des Systèmes Complexes, CNRS-Université de Provence, PIIM, Case 321, Av. Escadrille Normandie Niemen, 13397 Marseille, France.*

[3] *Association Euratom-CEA, DRFC-CEA Cadarache, 13108 St Paul-lez-Durance Cedex, France.*

A 2-dimensional numerical simulation of interchange instability in the scrape off layer (SOL) has already shown the existence of particle avalanches moving inward and outward. These avalanches result from the onset of long lived and radially extended convective cells. In the present study, we investigate the transport properties of a passive scalar in the presence of such avalanche events. Our statistical analysis shows that the predominant transport which results from interchange instability can be super-diffusive or even ballistic both inwards and outwards. So the large electric convection cells generated by plasma turbulence can lead to strong impurity influx even in regimes where avalanche transport is weak.

Introduction

The study of interchange instability in the scrape off layer has already shown the existence of particle avalanches in edge plasma turbulence. In [1] the non-linear evolution of such instability mechanisms is solved with a flux-driven model. In this new approach an external driving flux is imposed and there is no assumption of scale separability. The main assumptions of this fluid model are the flute hypothesis, i.e, perturbations are constant along the field lines (which allows a two dimensional treatment), constant temperature and a constant ion Larmor radius throughout the system.

At first we briefly present the flux-driven system used, and then we develop the statistical study made with test-particles to characterize the particle transport in avalanche-events, which appear in the scrape off layer (SOL).

Flux-driven system

The flux-driven system used relies on the density and charge balance equations which govern the non-linear evolution of the normalised density $N(x, y, t)$ and electric potential $\Phi(x, y, t)$, where x and y respectively refer to the radial and the poloidal

directions. That means the averaged system considered reads :

$$(\partial_t - D\nabla_\perp^2)N = [N,\Phi] - \sigma N \exp(\Lambda - \Phi) + S$$
$$\frac{g}{N}\partial_y N + (\partial_t - \nu\nabla_\perp^2)\nabla_\perp^2\Phi = [\nabla_\perp^2\Phi,\Phi] + \sigma(1 - \exp(\Lambda - \Phi))$$

where D and ν are the diffusion and the viscosity coefficients, Λ is the floating potential : $\Lambda = \ln(2m_i/(\pi m_e)^{1/2}$, σ the conductivity and g the curvature coefficient which takes into account the magnetic shear of the field lines. The non-linear term $\sigma N \exp(\Lambda - \Phi)$ represents the sheath current. $[N,\Phi]$ and $[\nabla_\perp^2\Phi,\Phi]$ are the Poisson brackets relative to the electric drift velocity and to the polarisation current. The treatment of the linear terms is made in the Fourier space by considering a periodic box in the two directions (radial and poloidal). The particle source term S is modeled by a Gaussian centered on the separatrix $x = (\frac{r-a}{\rho_s}) = 0$, (where a is the minor radius of the device), i.e $S(x) = S_0 \exp(-(\frac{x}{\lambda_s})^2)$ with typically $\lambda_s = Lx/30$, where $2Lx$ represents the radial box size (x ranging from $-L_x$ to L_x).
The transverse length scale is normalised to the ion Larmor radius $\rho_s = c_s/\Omega_0$ where Ω_0 and $c_s = \sqrt{T_e/m_i}$ are respectively the ion cyclotron frequency and the acoustic velocity. In the parallel direction, the scale is the connection length of the field lines between two limiters. Time is normalised to $1/\Omega_0$. Density is normalised to an arbitrary density n_0 and the electric potential to e/T_e.

Test-particles

In order to analyse the transport of particles moving in these fluctuating fields, we create an ensemble of 10000 particles, whose motion is given by the $\vec{E} \times \vec{B}$ drift, neglecting the polarisation drift. Therefore their radial and poloidal coordinates are the conjugated variables of the following Hamiltonian system :

$$\dot{x}(t) = -\partial_y\Phi(x,y,t), \;\; \dot{y}(t) = \partial_x\Phi(x,y,t). \tag{1}$$

The Hamiltonian of this autonom system is Φ, which is the electrostatic potential resulting from the numerical solution of driven-flux system presented before. The test particles are massless and do not perturb the electric potential, so that we can neglect Larmor radius effects and consider only the guiding center motion.
The following statistical study of the transport is based on the relation in time which exists for the mean square displacement of the particles. This relation is given by :

$$\left(\langle x^2\rangle - \langle x\rangle^2\right)(t) = Dt^\mu \tag{2}$$

where D is the diffusion coefficient and

$$\langle x^\alpha\rangle = \sum_{i=1}^{N} \frac{(x_i(t) - x_i(0))^\alpha}{N}$$

(with N the particle number and x_i the radial position of the ith particle). For a normal diffusion this mean square is proportional to the time, because $\mu = 1$ for classical random walk. If the parameter μ differs from one, the transport is called 'strange' (or sometimes 'anamolous'). The transport is called sub-diffusive when $0 < \mu < 1$

and super-diffusive when $1 < \mu < 2$. For $\mu = 2$ the particles move with constant velocity and the transport is ballistic.
So the main purpose of this paper is to characterise the transport in avalanche events, by evaluating this exponent μ. Here we focus our analysis on the mean square displacement in the radial direction, since this is the quantity which determines the confinement properties in a tokamak. The variance is computed with 10000 particles and μ is evaluated by interpoling $\log(\langle x^2 \rangle - \langle x \rangle^2)$ with the line $y = \mu \log t + b$, where $b = \log D$. This interpolation is based on an iterative least-square convergence. The motion equations (1), are solved numerically with a Runge-Kutta scheme of order 4 with a discretisation step equal to $10^{-1}/\Omega_0$. More and more often a Burlish-Stoer or a leap-frog scheme are prefered to a Runge-Kutta scheme (cf. [2]) for turbulent transport study, because they are simplectic. It has been proved that in some cases a simplectic algorithm is absolutely necessary (cf. [3]), because it assures area conservation. However Runge-Kutta is substantially faster than these methods and has been sufficient for our cases. We have verified that a Runge-Kutta scheme correctly reproduces the motion of a particle along a given isolated vortex.

Numerical analysis

In this simplified approach, the SOL geometry is a square box. The normalised coordinates x refers to the radial direction, while $y = a\theta/\rho_s$ labels the poloidal location of a field line at a given toroidal position. We consider a SOL created between two toroidal limiters located at symmetrical poloidal angles $\pm\Delta\theta$. The numerical values used correspond to standard characteristics of SOL plasmas : $T_e = 300keV$, $B_0 = 3T$, $R_0 = 2m$, $q = 3$ and $D_B = 30m^2s^{-1}$. D and ν are equal to 2×10^{-2} while the magnitude of the source term is $S_0 = 10^{-2}$. The radial and the poloidal sizes of the box are 128 ion Larmor radii. The integration time steps equals $\Delta t = 1/\Omega_0$ and the typical evolution time is of order of $10^4 \Delta t$. The flux-driven model is solved by a pseudo-spectral code where time integration is performed by a predictor-corrector scheme.

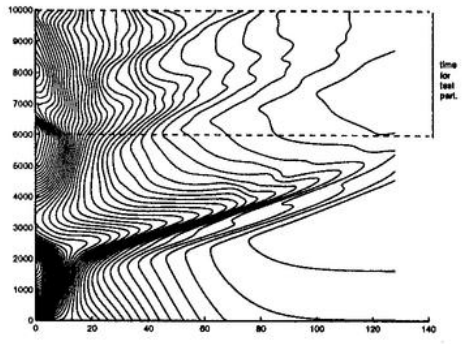

Figure 1: Iso-contour of density $N(x,t)$ as a function of the radial position and time, for $10^4/\Omega_0$.

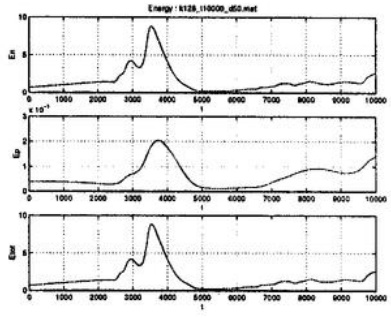

Figure 2: Energy averaged in the poloidal direction. The first plot is $\langle E_n \rangle_y = \langle N^2 \rangle_y$, the second is $\langle E_p \rangle_y = \langle |\nabla \Phi^2| \rangle_y$ and the last the total energy.

If we plot the iso-density contours representing the flux surface average of density profile (cf. fig1), we note deformations which correspond to super and sub-density

bursts. As already shown (cf. [1]), these avalanches result from the onset of long lived and radially extended convective cells.
The purpose of this paper was to study the behaviour of test-particles in such avalanche events. For this analysis we have study the test-particle evolution, by beginning at time $t = 6000/\Omega_0$, which corresponds to the time after the first non physical relaxation avalanche (cf. fig1), where the energy : $\langle E \rangle_y = \langle N^2 \rangle_y + \langle |\nabla \Phi|^2 \rangle_y$ begins to saturate (cf. fig2). As we are working on a finite system we have to use boundary conditions for the test particles. These are periodic in the poloidal direction and of absorption in the radial direction. The drawback of such an absorption condition is that after a certain time the particle number becomes too small to generate good statistics. For this reason the evolution time for the statistical results presented is of order of $2 \times 10^3 \Delta t$, which typically corresponds to the time the first particles need to reach the system boundaries (cf. fig3).
At first by considering individually the particle trajectories, we note that there are no closed trajectories, therefore no evidence for small convective cells (cf. fig4). Furthermore, the distance between two initially neighbouring particles may increase exponentially as expected. This inhomogeneous spatial character of transport is due to the potential map inhomogeneity. This transport is dominated by fast transverse events and the displacement can be either inwards or outwards.

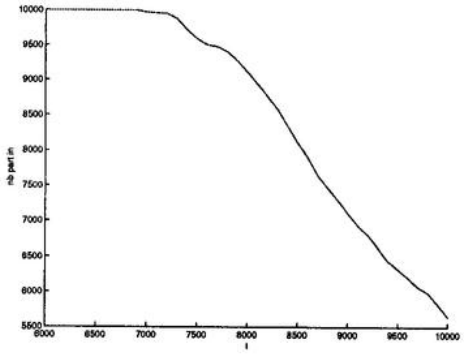

Figure 3: Evolution of the number of test particles number during $4000/\Omega_0 s$.

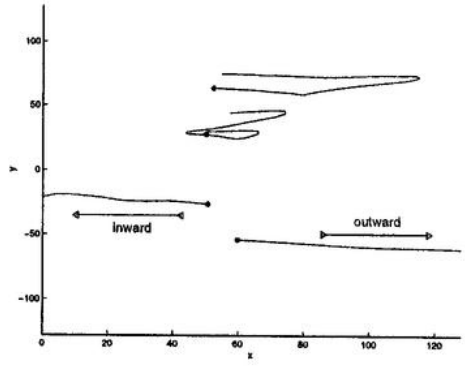

Figure 4: Trajectories in (x,y) of 4 individual particles during $4.10^3/\Omega_0 s$ (where the stars denote the initial position of each particle).

Now let us initially uniformly distribute the 10000 test-particles used for statistical analysis within a narrow vertical band and follow their space evolution in time (cf. fig5). It is important to note that the particles do not have a random repartition, but that they are on the contrary, concentrated around the vortices, avoiding the centers. It appears that particles first follow ballistic trajectories, whereas, in a second stage they diffuse slowly.

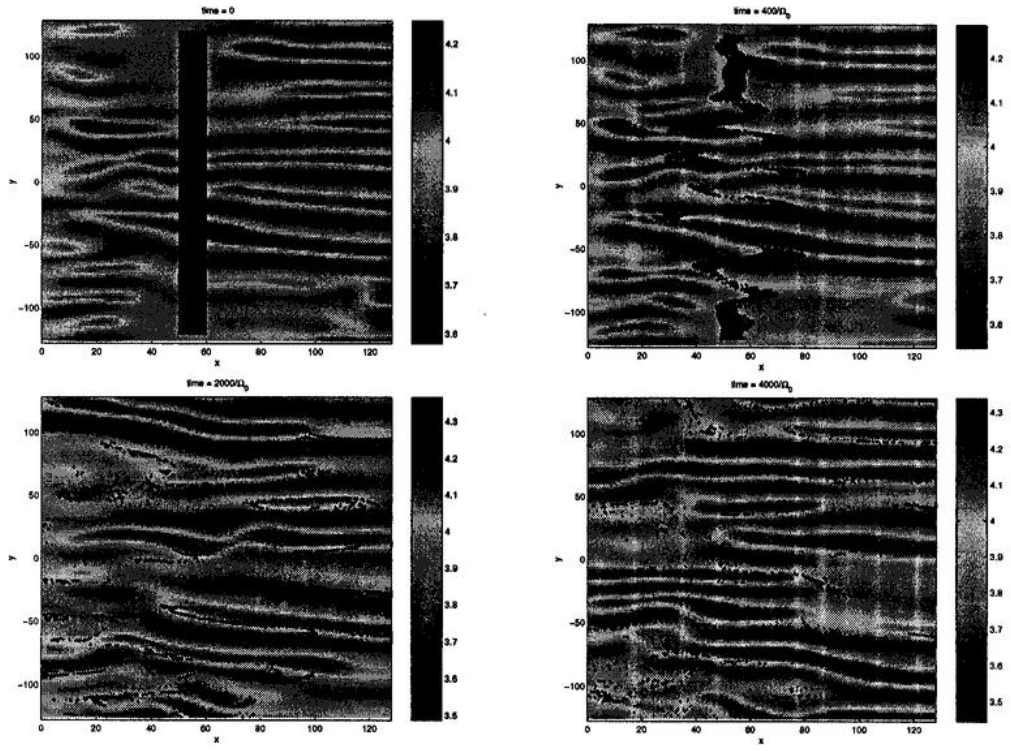

Figure 5: Superposition of the potential map with (x, y) position of 10^4 particles (black points). The first figure is the initial time, where particles are uniformely distributed on a band $(50 \leq x \leq 60); (-120 \leq y \leq 120)$. The 3 others correspond resp. to the $400/\Omega_0 s$, $2000/\Omega_0 s$ and $4000/\Omega_0 s$ times.

This behaviour is supported by the statistical study of the mean square displacement (cf. fig6). Indeed, we find that $\langle x^2 \rangle - \langle x \rangle^2$ is at first proportional to t^2 then to $t^{0.8}$. The transition from ballistic to sub-diffusive corresponds approximatively to the time where 10 percents of the particles have already reached the boundary. Due to finite size of the system, particles with a ballistic motion move out of the box after a finite time. After this point, these particles are no longer accounted for in the simulation. This gives a possible explanation of the transition to diffusive transport. The study of the particle distribution function (p.d.f) give more detail. For a normal random walk, the particle distribution should be Gaussian at large times. A measure of the proximity of distribution to a Gaussian can be given by its kurtosis $\kappa = \frac{\langle f^4 \rangle}{3\langle f^2 \rangle}$ and its skewness $s = \frac{\langle f^3 \rangle}{\langle f^2 \rangle^{3/2}}$ (where in our case $f = \Delta x - \langle \Delta x \rangle$). A Gaussian distribution has $\kappa = 1$, whereas a flatter distribution has $\kappa < 1$ and a more peaked, $\kappa > 1$. The skewness gives the same kind of information on the function width. So with a skewness between -0.2 and 0.4, for p.d.f evaluated at 6 different time steps during the first $10^3/\Omega_0 s$ (cf. fig7), we can definitely say that the global transport during avalanche events is 'strange' and not diffusive.

If we consider that the test particles correspond to a passive scalar embedded in a fluctuating field, they also describe well the motion of impurities, providing that these impurities are trace impurities. So the evidence of outward ballistic transport, could indicate a significative extension of the SOL. But conversely the existence of inward ballistic transport, gives the possibility of important plasma contaminations due to impurities generated by the wall.

A similar study has been made for $\nu = 10^{-2}$, $D = 10^{-2}$ and $S_0 = 5 \times 10^{-1}$. In this case the potential structures are less dominated by such long radial vortices and the avalanches are less important. The transport remains 'strange' (super-diffusive, with $\mu = 1.7$). This prove that impurities can move quickly inward and outward, even if the avalanche-events are weak.

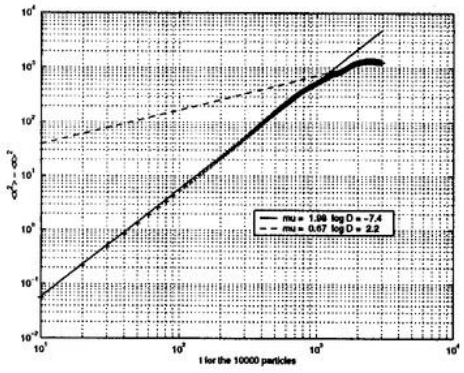

Figure 6: Time evolution of the mean squared radial displacement $\langle x^2 \rangle - \langle x \rangle^2$, for 10^3 particles. The crosses are the calculated values and the lines, the best interpolations calculated for the 2 slopes observed : $y = \mu x + \log D$.

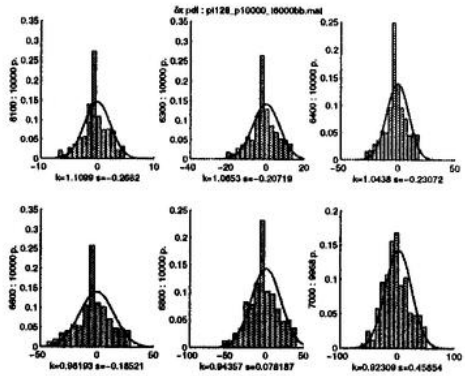

Figure 7: Normalised p.d.f of 10^3 particles for the radial variations with the initial positions for 6 different time steps during the first $10^3/\Omega_0 s$. k and s label the kurtosis and the skewness. The correspondant Gaussian is superimposed on each p.d.f.

Conclusion

We have studied the radial transport of test particles in turbulent flux-driven systems in presence of avalanche events. We note that the particles are not randomly distributed but concentrated on the potential structure. The size of these structures is comparable to the system size. A statistical study has permitted us to characterise the transport, which is dominated by ballistic events. This transport, whose characteristic time scale is very short, can be both outward and inward. The analogy which can be made between test-particles and trace impurities, reveals that impurity transport can be advantageous. But conversely, the existence of ballistic trajectories into the discharge demonstrates the possibility of strong plasma contamination due to impurities generated by the wall.

References

[1] Y. Sarazin and Ph. Ghendrih, Physics of plasmas, vol. 5, n. 12, 1998.

[2] S.V. Annibaldi, G. Manfredi, R.O. Dendy and L.O'C. Drury, PPCF, vol. 42, n. 4, 2000.

[3] R.I. McLachlan and P. Atela, Nonlinearity 5, 541-562, 1992.

Dependence of internal kink growth rate on tokamak plasma current and shape parameters

An. Martynov, O. Sauter

Centre de Recherches en Physique des Plasmas,

Association EURATOM-Confédération Suisse,

Ecole Polytechnique Fédérale de Lausanne,

CH-1015 LAUSANNE, Switzerland

Introduction

The ideal internal kink mode is one of possible triggers of sawtooth oscillations [1] and it is important to know the stability of ideal internal kink to be able to predict the behavior of sawteeth.

The numerous theoretical studies of the internal kink behavior in tokamak plasmas have provided several analytical approximations for the dependence of the internal kink growth rate on plasma parameters. These approximations are obtained for the standard parabolic profiles and only elongation is taken into account. However the experimental results of TCV tokamak show that the sawtooth activity depends on elongation and triangularity [2].

The real plasmas of TCV tokamak are well beyond the mentioned constrictions and the behavior of ideal kink mode should be studied by means of numerical ideal MHD codes. Aiming at a better understanding of internal kink stability and, thus, of sawteeth activity in TCV plasmas, we have undertaken the study of the dependence of the internal kink stability on plasma shape and current in a wide range of these parameters. The first results let us to propose some corrections to the analytic formulae allowing a better description of the dependence on triangularity

2. Analytic formulae for internal kink.

There are several theoretical works giving analytical approximations of dependence of the ideal internal kink growth rate on different plasma parameters [3, 4, 5]. The summary of several of them is given in [1]. The theoretical analysis gives formulae for the normalized variation of the potential energy of perturbation $\delta\hat{W}$ and the growth rate

of instability can be obtained as $\gamma = \delta\hat{W}/\tau_A$, where Alfven time $\tau_A = \sqrt{3}\,R/\upsilon_A$, R is the major radius and υ_A is Alfven speed. There is the well-known expression obtained by Bussac et al [3] in 1975 (in the form cited in [1]):

$$\delta\hat{W}_{Bussac} = -\frac{9\pi}{s_1}(l_{i1} - \frac{1}{2})\varepsilon_1^2(\beta_{p1}^2 - \beta_{pc}^2) \qquad (1)$$

where

$$\beta_{pc} = 0.3(1 - \frac{5}{3}\varepsilon_1)\,,\ \beta_{p1} = \beta_{Bussac} = \frac{8\pi}{B_{pl}^2}(\langle p\rangle_1 - p(r_1))\,,$$

s_1, l_{i1} and ε_1 are the magnetic shear, internal inductance and aspect ratio on q=1 surface, B_{pl} is the poloidal magnetic field on q=1 surface. The elongation term is given by [4]

$$\delta\hat{W}_{el} = -\frac{18\pi}{s_1}(l_{i1} - \frac{1}{2})^3(\frac{\kappa_1 - 1}{2})^2 \qquad (2)$$

where κ_1 is elongation on q=1 surface. Another approximation is given by [5]

$$\delta\hat{W}_{\kappa} = -\frac{3}{4}(\kappa_1 - 1)\beta_{p1} + (q_0 - 1)\left[\frac{13}{48} - 3\beta_{p1} + \frac{\kappa_1 - 1}{2}(13\beta_{p1}^2 - \frac{1}{4}\beta_{p1} - 1)\right] \qquad (3)$$

Note that these formulae are obtained for parabolic safety factor profiles and for circular or elongated cross-sections, when the triangularity is not taken into account.

3. **Parameter range and methodology of the calculations**

TCV (Tokamak à Configuration Variable) is the medium-size machine, designed especially to explore various plasma configurations. The basic features of TCV are the unique flexibility, allowing to explore the behavior of plasmas in a very wide range of shape parameters: elongation up to 2.8 and triangularity between -0.7 and +0.9. These shapes, especially the cases with high triangularity, are beyond the conditions for which the analytic approximations of internal kink have been obtained.

Another important feature of TCV is the unique system of EC heating and current drive, including 6 independently controlled adjustable power launchers, providing the launch of 3 MW of microwave power on 2nd EC harmonics in the desired configuration. Using these launchers, various non-parabolic current profiles are obtained on TCV, including reversed shear configurations. Thus, both shape and current profiles in TCV

The equlibria were calculated by CHEASE code [7], mapped and used in KINX code calculations of internal kink mode stability. Approximately 2000 calculations were performed.

We have compared the results of calculations with the formula, proposed in [1]: $\delta\hat{W}_{shape} = \delta\hat{W}_{Bussac} + \delta\hat{W}_{el}$. There is a general agreement of the calculated data with theory, but there are some points where the calculated internal kink growth rate is far from predicted by analytical expressions. The growth rates obtained for equlibria with non-parabolic profiles proved to be often higher or lower than the analytical predictions. There is also a scattering of calculated points around the analytic value (Fig. 1).

The role of the most important parameter which is not included in the analytic formulae, triangularity, is shown in Fig. 2. The approximative formula

$$\gamma_{calc} = \frac{(\delta\hat{W}_{Bussac} + \delta\hat{W}_{el})}{\tau_A} \cdot 16 \cdot \left((\delta_1 + 0.128)^{0.4}(0.105 - \delta_1)^{0.4}(0.5 - \delta_1)\right) \qquad (4)$$

describes well the dependence of internal kink growth rate on triangularity for edge elongations exceeding 1.5. For lower elongations the equilibria used in calculations proved to be stable. Note that at zero triangularity the calculated values are exceeding the analytic predictions for the factor of ~1.4. The proposed approximation is valid only for the unstable region and describes well the behavior of growth rate on the limits of the unstable region at high positive or negative triangularity. The calculations show that the high positive or negative triangularity is stabilizing the ideal internal kink mode and at high enough values of triangularity ($\delta_1 > 0.105$ ($\delta_{edge} > 0.8$) and, admittedly, $\delta_1 < -0.13$ ($\delta_{edge} < -0.9$) - the calculations did not reach the negative triangularities below $\delta_{edge} < -0.8$) the ideal kink mode can be stabilized.

On figure 3 the comparison of calculated internal kink growth rate with the analytical predictions multiplied by the correction factor is presented. It is seen that with this correction most part of our results correspond to the analytical formula.

Conclusions

The values of the internal kink growth rate calculated by KINX code for parabolic q profiles are in general agreement with analytical predictions.

There is a clear dependence on triangularity confirming the experimental results [2]. The dependence of calculated internal kink growth rate on triangularity in the range of $-0.08 < \delta_1 < 0.12$ can be satisfactorily described by multiplying the analytical prediction by the correction coefficient, giving the following formula:

$$\gamma_{calc} = \frac{(\delta\hat{W}_{Bussac} + \delta\hat{W}_{el})}{\tau_A} \cdot 16 \cdot \left((\delta_1 + 0.128)^{0.4}(0.105 - \delta_1)^{0.4}(0.5 - \delta_1)\right)$$

The calculations have shown that the high positive or negative triangularity is stabilizing the internal kink mode.

The work will be continued and the plans are as follows:

We are going to study the role of other parameters, including the domain of non-parabolic current profiles - they require a more serious study. The set of q profiles used in calculations will be modified to get the independent variation of q profile parameters; the dependence of internal kink growth rate on triangularity with low elongation (in present calculations most of these cases proved to be stable) will be investigated by increasing β_{p1}. The low β_{p1} cases with high elongation will be studied because these cases can prove to be unstable with low or zero β_{p1}. We are also going to compare the results of calculations and the obtained dependencies with TCV experimental data and to modify the sawtooth crash model used for sawteeth simulation. The studies of the resistive kink mode which can be triggering the sawtooth oscillations when the ideal mode is stable, are also planned.

References

1 *F. Porcelli et al, Plasma Phys. Control. Fusion* ***38*** *(1996) 2163-2186*

2 *Reimerdes H et al, Plasma Phys. Control. Fusion 42 (2000) 629-639*

3 *Bussac M N et al, 1975 Phys. Rev. Lett.* ***35*** *1638*

4 *Lutjens H, Bondeson A and Vlad G, 1992 Nucl. Fusion* ***32*** *1625*

5 *Wahlberg C, 1998 Phys. Plasmas* ***5*** *1387*

6 *Degtyarev L, Martynov A. A., Medvedev S, Troyon F, Villard L, Gruber R 1997 Comput. Phys. Commun.* ***103*** *10*

7 *H. Lutjens, A. Bondeson, O. Sauter, LPR 545/96*

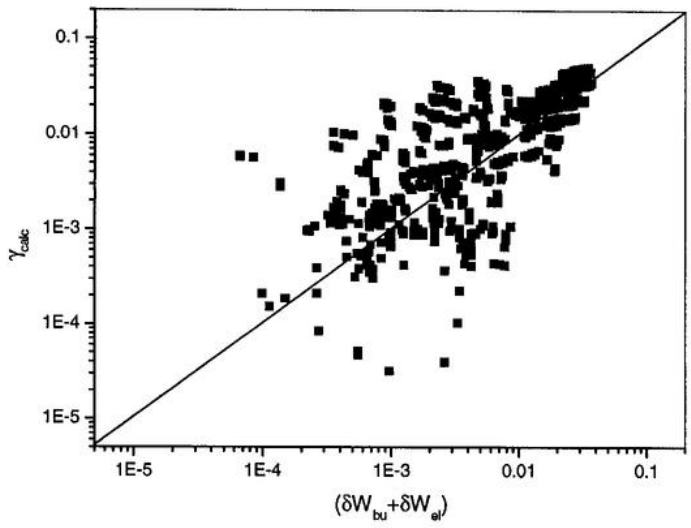

Figure 1. The comparison of calculated internal kink growth rate with analytical predictions.
The scatter is concerned with differences in triangularity and with non-parabolic current profiles.

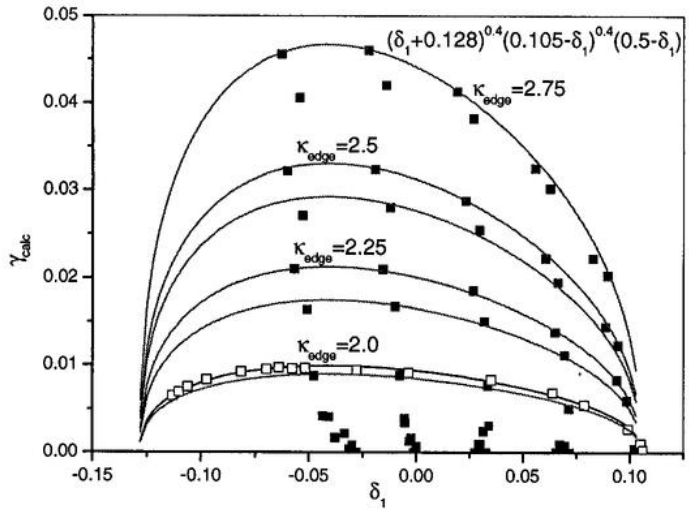

Figure 2. Dependence of the calculated growth rate on triangularity at different elongations and the fit used for description of this dependence. The formula of fit is shown on the picture (the fit is valid for cases with κ_{edge}>1.5, the lower κ has yet to be studied)

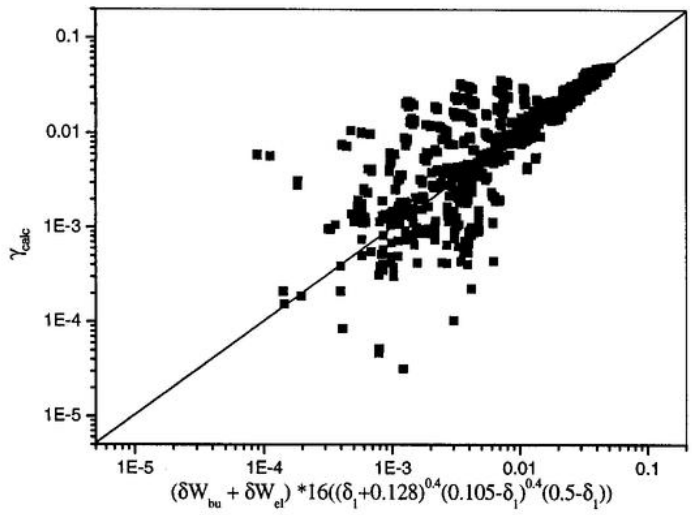

Figure 3. The comparison of the calculated growth rates with the modified scaling. The remaining scatter of point is concerned with non-parabolic current profiles (to be studied).

Numerical and experimental studies of electron cyclotron current drive efficiency in plasmas with nearly zero ohmic current

P. Nikkola and O. Sauter

Centre de Recherches en Physique des Plasmas, Association Euratom - Confédération Suisse, Ecole Polytechnique Fédérale de Lausanne PPB, CH-1015 Lausanne, Switzerland

Abstract. In the TCV tokamak, it is possible to create steady-state discharges with full current replacement by electron cyclotron current drive (ECCD) [1]. In this work, we estimate the EC driven current with various launching angles and compare experimental and theoretical methods to reveal the ECCD component. Also, differences between experimental and theoretical values of current drive efficiency and plasma conductivity are discussed in discharges with a small or vanishing induced electric field.

1. Introduction

The microwave system of the TCV tokamak is constituted by 6 gyrotrons (frequency 82.7 GHz; total power close to 3 MW) which couple to the second harmonic of the electron cyclotron frequency of the plasma. In order to drive current, the microwaves are launched into the plasma with a finite toroidal launching angle, $\varphi_T \neq 0°$. With the launchers of TCV, it is possible to drive current in the same direction as the Ohmic plasma current, CO-CD, or in the opposite direction, CNT-CD. As has been recently shown, full current replacement can be achieved already with three gyrotrons, power of about 1.35 MW. The ECCD efficiency is defined as

$$\eta_{CD} = I_{CD}/P_{abs} \tag{1}$$

where I_{CD} is the current driven by microwaves and P_{abs} is the absorbed power. In steady state, the total parallel plasma current is the sum of the following components

$$I_P = \hat{\sigma} V_{loop} + I_{BS} + I_{CD} \tag{2}$$

where the global plasma conductivity is

$$\hat{\sigma}_{neo} = \frac{T(\psi_a)}{4\pi^2} \int_0^{\psi_a} \frac{< 1/R^2 >}{T} \sigma_{neo}\, dV. \tag{3}$$

The total bootstrap current and the current generated by microwaves can be expressed in terms of the current densities as

$$I_{BS} = \frac{T(\psi_a)}{4\pi^2} \int_0^{\psi_a} \frac{< \mathbf{j}_{BS} \cdot \mathbf{B} >}{T^2}\, dV \tag{4}$$

$$I_{CD} = \frac{T(\psi_a)}{4\pi^2} \int_0^{\psi_a} \frac{< \mathbf{j}_{CD} \cdot \mathbf{B} >}{T^2}\, dV \tag{5}$$

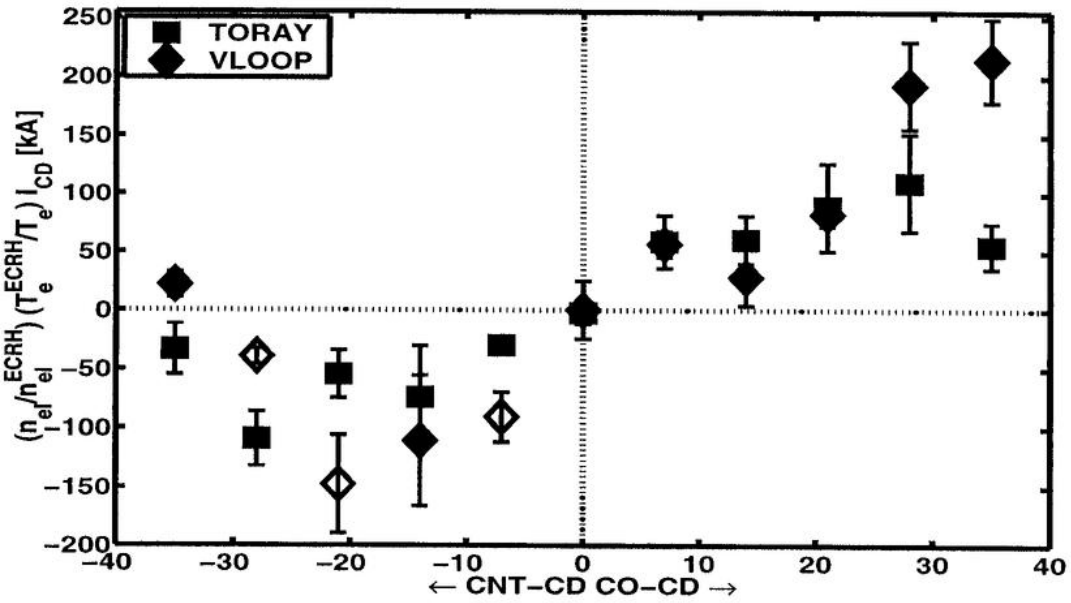

Figure 1. Dependence of I_{CD} on the toroidal launching angle as obtained with two methods. Horizontal axis is the toroidal launching angle, φ_T. Note the normalization of I_{CD}.

respectively. Above, $T(\psi) = RB_\phi$, R is the major radius, B_ϕ is the toroidal magnetic field, ψ_a is the poloidal magnetic flux at the plasma boundary, σ_{neo} is the local neoclassical plasma conductivity, and $< \ldots >$ means flux surface average. The flux surface averaged bootstrap current and the neoclassical conductivity are calculated according to [2].

2. Launching angle scan

A scan in the launching angle was made in order to find the optimum value for φ_T. In the experiments, the launching angle was varied between $\pm 35°$ with steps of 7°. Three gyrotrons were switched on at 0.2 s with a total output power between 1.30 MW and 1.40 MW. Conditions were kept constant for 0.45 s. Thomson measurements were averaged over a time interval of about 100 ms in order to reduce effects of local fluctuations in the data. For these reasons, the plasma had about 300 s to reach steady-state. This time is much larger than the energy confinement time and more than twice the current redistribution time, at least for the CO-CD launch.

In Fig. 1, we show the EC driven current as a function of the toroidal launching angle for 11 discharges. The current is calculated with two methods as follows. 'TORAY' means results form the linear, relativistic ray-tracing and current drive code [3,4] using experimental profiles. In the 'VLOOP' method, the change in the loop voltage, with respect to the heating-only ECH discharge, $\varphi_T = 0°$, gives directly the driven current if the plasmas are similar, i.e., same I_P and I_{BS}. In this case, we can write for I_{CD}

$$I_{CD}^{VLOOP} \approx C\left(T_{ECH}^{3/2} V_{ECH} - T_{e0}^{3/2} V_{loop}\right) \tag{6}$$

where T_{e0} is the maximum electron temperature, V_{loop} is the measured loop voltage, and the subscript 'ECH' refers to the heating-only discharge. The constant C, proportional to conductivity, can be found from the ECH reference shot as $C = (I_{PECH} - I_{BSECH})/(V_{ECH} T_{ECH}^{3/2})$.

Because the current drive efficiency depends on the local plasma parameters as

$$\eta_{CD} \sim \frac{T_e}{n_e R(Z_{eff}+5)} \tag{7}$$

the currents in the figure are multiplied by $(T_{e0ECH}/T_{e0})(n_{el}/n_{elECH})$ to compensate for small differences in temperature and density between discharges. The TORAY code gives full first pass absorption in all cases except for the largest angles ($\varphi_T = \pm 35°$), where only about half of the power is absorbed. The total plasma current was between 167 kA and 177 kA and the density was between $1.75 \times 10^{19}\mathrm{m}^{-3}$ and $1.9 \times 10^{19}\mathrm{m}^{-3}$, except for plasmas with $\varphi_T = -14°$ and $-21°$ in which the density was $1.6 \times 10^{19}\mathrm{m}^{-3}$ and $1.5 \times 10^{19}\mathrm{m}^{-3}$, respectively. Temperature was between 4.8 keV and 5.6 keV except discharges with $\varphi_T = +28°$ and 35° were somewhat colder, 3.2 keV and 3.5 keV, respectively. In addition, three CNT-CD plasmas were wery hot, namely plasmas with $\varphi_T = -7°$, $-21°$, and $-28°$ had temperatures of 9.1 keV, 7.1 keV, and 8.2 keV, respectively. These hot plasmas are marked with an open symbol.

In the CO-CD case, both methods agree within error bars, except for the largest angle. Estimating the electric field strength, we notice that we are well in the nonlinear regime according to [5]. TORAY systematically gives higher current than the experimental method. This can be due to $Z_{eff} = 3.5$ used in the calculations being too low. At the largest angle, $\varphi_T = 35°$, I_{CD}^{TORAY} is much smaller than I_{CD}^{VLOOP}, even if we assume full first pass absorption. If we calculate the bootstrap current using experimental profiles according to Eq. (4), we get for the Ohmic current a value $I_{OH} = 38$ kA. With the measured $V_{loop} = 0.101$ V, the plasma conductivity is about 380 kA/V. This is quite close to the calculated value, $\hat{\sigma}_{neo} = 340$ kA/V assuming $Z_{eff} = 3.5$. This suggests that I_{CD}^{VLOOP} is closer to the actual I_{CD} with $\varphi_T = 35°$. The low I_{CD}^{TORAY} can very well be related to relatively larger nonlinear effects in the cold plasma region. X-ray measurements have confirmed the formation of a high energy tail with $|\varphi_T| > 0$ and no tail with $\varphi_T = 0$ [6]. Therefore we expect a large tail at larger angles and, consequently, a larger discrepancy with TORAY. The temperature at the absorption location, as calculated with TORAY, for $\varphi_T = 21°$ and 28°, is 3.7 keV and 2.2 keV, respectively. As a conclusion, the largest launching angle is the most beneficial for the current drive.

With CNT-CD the situation is different. The relaxation time of 300 ms may not be long enough since the shape of the current profile starts to change considerably from the Ohmic state when the EC power is switched on. Thus, the assumption of stationarity of the discharges is not correct. In addition, the plasmas are much hotter, with temperatures up to 9.1 keV, than in the ECH discharge with $T_{e0}^{ECH} = 5.2$ keV. The reason for the large temperature is better confinement due to lower shear in the plasma centre [7]. This implies more peaked profiles for the hottest plasmas, violating the assumption of similar plasmas required for the VLOOP method. Here, we can not expect the VLOOP method to be applicable. The measured profiles in the CNT-CD cases had strong fluctuations, so that the real profiles can differ considerably from the ones used in TORAY.

One should note that, for cases with $\varphi_T = -14°$ and $-21°$, V_{loop} is very high, 0.74 V and

0.68 V, respectively. These are also the discharges with the lowest densities. It is well possible that a large Ohmic current is present in the plasma implying a large EC current in the counter direction. The value of I_{CD}^{VLOOP} for $-14°$ is about 110 kA. The temperature of this discharge is only 5.1 keV, about the same as for ECH. If we assume that the profiles for these cases are similar, and estimate the conductivity as $\hat{\sigma}_{-14°} \approx CT_{e0}^{-14°} = 380$ kA/V we get for the Ohmic current a value 280 kA. With the calculated $I_{BS} = 13$ kA and the measured $I_P = 170$ kA, we get $I_{CD}^{-14°} = -97$ kA, close to $I_{CD}^{VLOOP} = -107$ kA. The value of I_{CD}^{TORAY} is -76 kA. Thus, I_{CD}^{VLOOP} is probably closer to the actual I_{CD}. The discharge with $\varphi_T = -21°$ is hot and the profiles can be very different from the ECH plasma, making the above estimation of the conductivity invalid. Because the density is even lower than in the discharge analyzed above, we can suspect an even larger counter I_{CD} component. The failure of TORAY is most probably due to poor profile measurements for this plasma.

The case with $\varphi_T = -28°$ has strongly fluctuating Thomson data and the temperature is also very high. Thus, both methods have problems and it is hard to justify which is closer to the actual value of I_{CD}. The discharge with $\varphi_T = -35°$ is somewhat colder than the ECH case, $T_{e0} = 5.0$ keV, suggesting that the profiles are not very peaked. The drop in I_{CD} in this case is not fully understood. It is possible that the first pass absorption is not complete. Another mechanism which could reduce I_{CD} is the direction of the DC electric field which is opposite to the driven current. The formation of the hot electron tail enhances the global plasma conductivity because of lower collisionality of the hot electrons [8]. Therefore, the Ohmic current may be under estimated for large angles which could in particular increase I_{CD} in the $-35°$ case and decrease it with $\varphi_T = +35°$. The absorption temperature was approximately the same as in the CO-CD case with the largest angle.

3. Measurement of $\hat{\sigma}$ and η_{CD}

Recently, full current replacement with ECCD has been achieved in the TCV tokamak [1]. The plasma was kept in steady state for more than 900 confinement times and more than 10 current redistribution times, the only limitation being the pulse length of the three gyrotrons, 2s. In order to avoid disruption due to too peaked profiles, the EC power was distributed along the minor radius and $\varphi_T = 35°$ was used to maximize efficiency. In this section, we analyze discharges of this campaign to estimate the plasma conductivity and current drive efficiency and compare the results with a linear theory.

In Fig. 2, we plot the total plasma current vs. loop voltage, Eq.(2). Both I_P and V_{loop} are multiplied by the line-averaged density to scale out the density dependence in η_{CD}, see Eq. (7). The values fit very well on the line implying similar plasmas. The bootstrap current was calculated to be approximately the same for all shots. From the slope of the fitted line we get for the experimental estimate of the plasma conductivity $\hat{\sigma}_{exp} = 710$ kA/V. Calculating the neoclassical conductivity, Eq. (3), with $Z_{eff} = 3.5$, we get $\hat{\sigma}_{neo} = 360$ kA/V. In order to get an agreement between theory and experiment, $Z_{eff} < 2$ is required. The value of Z_{eff} is hard to know accurately but if we assume that the only impurity species is carbon,

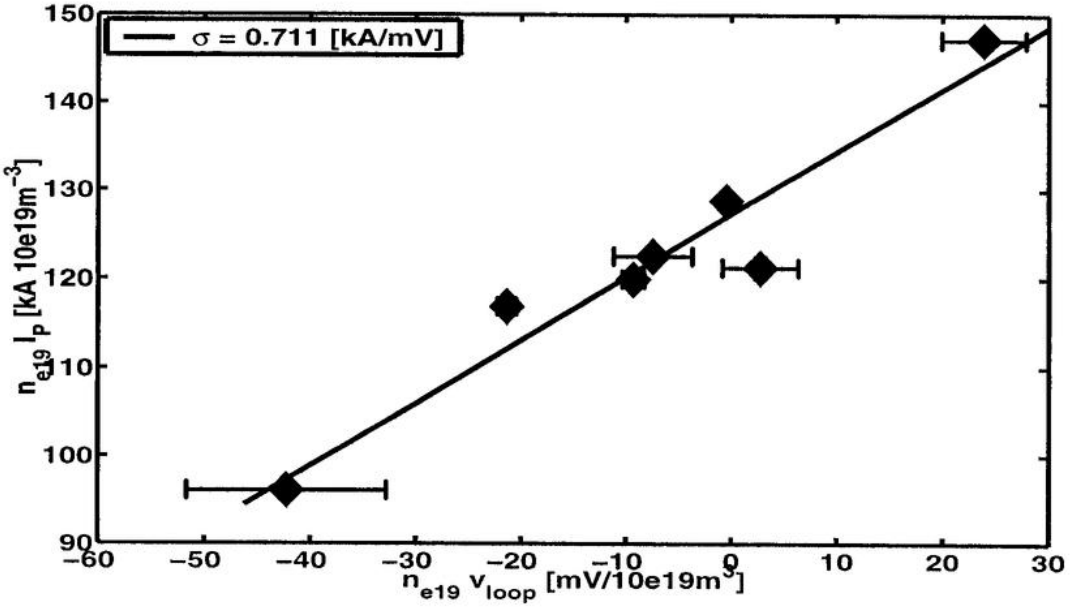

Figure 2. Experimental evaluation of the global plasma conductivity.

which is close to reality because the first wall of TCV is fully covered with carbon tiles, Z_{eff} is measured to be about 5. Although in ECCD discharges heavier elements have been observed, namely tungsten, which would cause an overestimation of Z_{eff}, it is improbable that it would be as small as 2. The remaining discrepancy between theory and experiment is most probably related to the hot electron contribution to the conductivity, see Chapter 2. In the neoclassical calculations a Maxwellian plasma has been assumed.

The experimental value of plasma conductivity was used to compute the Ohmic part of the plasma current. In all shots, the loop voltage is small so that the measurements are not sensitive to errors in the plasma conductivity. Subtracting I_{OH} and I_{BS}, which was calculated to be between 15 % and 26 % of the total plasma current, we get an experimental value for η_{CD}. In Fig. 3 we compare the experimental and TORAY values of η_{CD}. An error of 25 % for both I_{BS} and $\hat{\sigma}_{exp}$ was assumed and the error of V_{loop} was estimated from the extreme values of a line fitted in the V_{loop} signal, the latter giving the greatest contribution to $\Delta\eta_{CD}^{exp}$. The errorbars for the TORAY results are large due to large oscillations in the Thomson data. The results are in good agreement, although TORAY systematically underestimates the efficiency. The difference can be explained by the current carried by the hot electron tail, which is neglected in the linear code. The 'STEADY STATE' method, shown as open circles in the figure, is based on neoclassical calculation of I_{CD} through Eqs. (1)−(5), using experimental profiles. The method agrees very well with the experimental evaluations, even though $\hat{\sigma}_{neo}$ is lower than $\hat{\sigma}_{exp}$, because V_{loop} is small.

4. Conclusions

A series of ECCD discharges with a launching angle scan has been analyzed. Experimental values of I_{CD} and results from a linear, relativistic ray-tracing and current drive code have

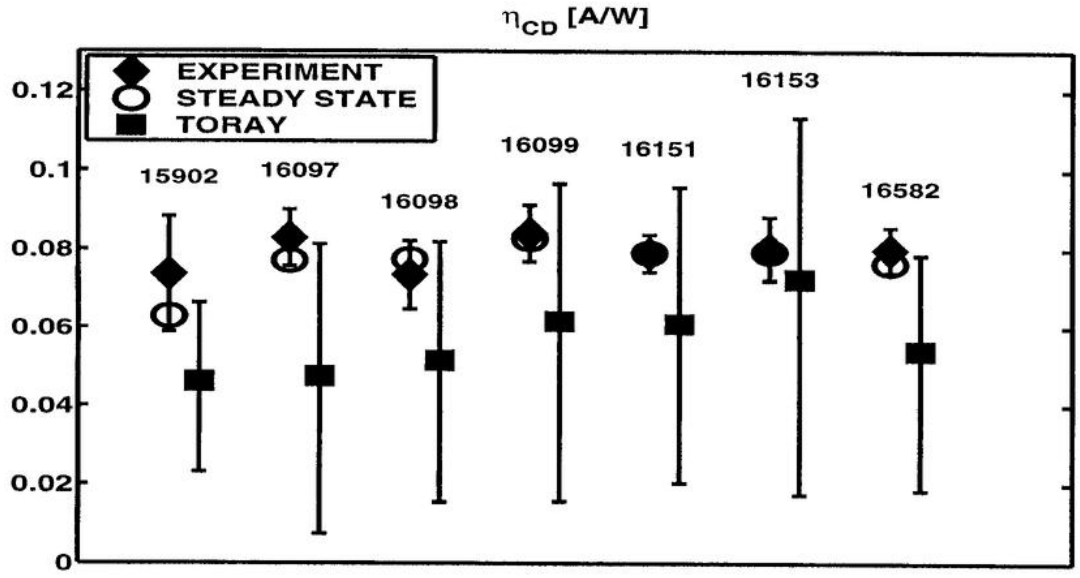

Figure 3. Comparison between experimental and TORAY values of ECCD efficiency.

been compared. The optimum launching angle for CO-CD was found to be the largest used, $\varphi_T = 35°$. The linear code gives relevant results except for the largest angle for which it predicts a very small I_{CD} mainly due to incomplete absorption. Also, the effect of the hot electron tail can be more important in this case because of colder plasma in the absorption location. In the CNT-CD discharges, both methods had problems due to poor profile data and variations in confinement, as compared to the ECH reference shot. In addition, an experimental value for the plasma conductivity was evaluated, with a value of $\hat{\sigma}_{exp} = 710$ kA/V. This is much larger than the neoclassical conductivity, $\hat{\sigma}_{neo} = 360$ kA/V. The difference can be attributed to the hot electron tail in the presence of EC power, which enhances the plasma conductivity. Also, experimental values of current drive efficiency were compared with the results of the linear code for shots with nearly zero Ohmic electric field. It was found that the linear code is close ot the experimental evaluation but slightly underestimates the current drive efficiency, possibly due to neglected hot electron tail.

This work was partly supported by the Swiss National Science Foundation.

6. References

[1] O. Sauter *et al,* Phys. Rev. Lett. **84** (2000) 3322.
[2] O. Sauter *et al,* Phys. Plasmas **6** (1999) 2834.
[3] G.R. Smith *et al,* Proc. 9th Joint Workshop on ECE and ECRH, Borrego Springs, California (Jan 1995), Editor World Scientific (1995) 651.
[4] R.H. Cohen, Phys. Fluids **30** (1987) 2442.
[5] R.W. Harvey *et al,* Phys. Rev. Lett. **62** (1989) 426.
[6] S. Coda *et al,* Proc. 26th EPS Conf. on Cont. Fusion and Plasma Physics, Maastricht 1999, Europhys Conf. Abstr. (1999) **23J** 1097.
[7] Z.A. Pietrzyk *et al,* Phys. Plasmas **7** (2000) 2909.
[8] N.J. Fisch, Phys. Fluids **28** (1985) 245.